Design and Testing of an Active Aircraft Wing Spar with Bending-Torsion Coupling

by

Carlos Manuel Baptista Pereira da Silva
Licenciatura Aeronautical Engineering, Portuguese Air Force Academy, 2002

A Thesis Submitted in Partial Fulfillment of the
Requirements for the Degree of

MASTER OF APPLIED SCIENCE

in the Department of Mechanical Engineering

University of Victoria

Design and Testing of an Active Aircraft Wing Spar with Bending-Torsion Coupling

by

Carlos Manuel Baptista Pereira da Silva
Licenciatura Aeronautical Engineering, Portuguese Air Force Academy, 2002

Supervisory Committee

Dr. A. Suleman, (Mechanical Engineering)
Supervisor

Dr. M. Bahrami, (Mechanical Engineering)
Department Member

Dr. C. Crawford, (Mechanical Engineering)
Department Member

Dr. F. Gebali (Electrical and Computer Engineering)
External Examiner

Supervisory Committee

Dr. A. Suleman, (Mechanical Engineering)
Supervisor

Dr. M. Bahrami, (Mechanical Engineering)
Department Member

Dr. C. Crawford, (Mechanical Engineering)
Department Member

Dr. F. Gebali (Electrical and Computer Engineering)
External Examiner

ABSTRACT

An experimental investigation on active aeroelastic aircraft structures with bending-torsion coupling properties is presented. Two techniques for vibration and flutter alleviation are studied and tested. The passive approach is based on the use of carbon composite spars with misaligned fibres. The second technique involves an active spar with a multi-cross section embedded with PZT actuators. A wing was designed and manufactured for testing in a wind tunnel and subsequently implemented on a demonstrator platform for flight testing.

Results show that a carefully designed misalignment of the fibres can lead to significant performance increase. The active system based on PZT actuators with a linear controller exhibits significant improvements in aeroelastic performance compared to the passive system. The research findings lead to the conclusion that significant vibration reduction and flutter envelope extension can be achieved using the proposed strategies.

TABLE OF CONTENTS

LIST OF TABLES

LIST OF FIGURES

LIST OF ACRONYMS

BTC - *Bending Torsion Coupling*

FEM - *Finite Element Model*

GVT - *Ground Vibration Test*

PID - *Proportional Integral Derivative*

PMN - *Lead Magnesium Niobate*

PVDF - *Polyvinylidene Fluoride*

PZT - *Lead Zirconate Titanate Piezoelectric*

RPV - *Remote Piloted Vehicle*

SHM - *Structural Health Monitoring*

SMA - *Shape Memory Alloys*

UAV - *Unmanned Aerial Vehicle*

ACKNOWLEDGEMENTS

First of all, I am thankful to the *Portuguese Air Force* and the *Fundação para a Ciência e a Tecnologia* for giving me the opportunity to perform this research towards my graduate degree. During this project, I had the precious support of several people, to whom I am very grateful. To Dr. Afzal Suleman, for the opportunity of joining his research team, for his support and mentoring. To my colleague, Eng. Bruno Rocha, for all the time he spent helping me. To Captain Costa, for his master craftsman capabilities to build the models and for piloting the flight test vehicle.

This work would not have been possible if it were not for all the previous research carried within the research group, namely the flight test platform and the electrical components. For this I am thankful to Dr. Paulo Moniz and Eng, Joana Rocha, to the Lieutenants Bruno Carreiro and Pinheiro, to Sergeant Ramos, to the Aeronautical Laboratory staff at the Air Force Academy who directly and indirectly supported this project, namely LtCol. Pedro Costa, Captains Delfim Dores and Maria Madruga, Sergeants Fernandes, Bandeiras and Rodrigues, Corporal Filipe and D. Fernanda.

Lastly, I show my gratitude to all my family members, my girlfriend Vanda and my goddaughter Beatriz, for supporting me all times, especially during my absence while studying in Canada.

To my parents and in memory of my grandparents,

CHAPTER 1

INTRODUCTION

Structural health condition monitoring of aircraft structures requires complicated, long and expensive maintenance operations. Therefore, there is a tendency in the air transport industry to reduce the number of these inspections to a minimum. Also, there are structural areas that are not readily accessible, implying decommissioning of the aircraft for long periods (for inspection and maintenance purposes). This increases the probability of significant damage developing between inspections and reduces aircraft reliability.

Methods to improve aircraft reliability include vibration suppression and real time health monitoring systems. Vibration reduction implies damage, wear and failure probability reduction, resulting in larger intervals between maintenance operations. Real-time structural health condition and monitoring implies abandoning corrective and preventive maintenance plans for predictive and proactive maintenance operations. Currently, passive measures are used to ensure aircraft reliability such as incorporating safety factors and redundancy in the design. Active methods offer an alternative that may result in a decrease in added weight (compared to the passive methods) with associated advantages such as less induced drag (if one considers that less lift will have to be generated), reduced fuel consumption, cost and pollution.

The objective of the current research is to design a wing spar with a continuous filament multi-cell cross section with bending and torsion coupling and integrated PZT actuators to control the vibration response. The proposed technology may have implications in aircraft design such as fatigue life extension and improved reliability.

It is noted that the directly targeted types of aircraft capable of taking advantage from the propose research are essentially small aircraft, such as remotely piloted vehicles and unmanned aerial vehicles and light airplanes as they share the common aspect of being usually designed with wings that have one main spar.

1.1 Active Aeroelastic Control

Aeronautic structures are flexible, specially the lifting surfaces. As the airplane is flying, structural deformation takes place. This leads to a change on the aerodynamic loads produced by them, due to the shape modification. The aerodynamics forces increment/decrement consequently results in a new structural deformation. This a two-way interaction between the structure and the fluid [1]. The behaviour can be stable, if an equilibrium condition is attained, or unstable, where catastrophic failure can occur.

Static aeroelasticity such as divergence is mass independent and is solely related to the structural elastic and aerodynamic forces. Dynamic aeroeslaticity is mass dependent and it is a self-sustaining vibration that occurs when the structure is initially deformed. If the aerodynamic load decreases, the structure responds by reducing its deformation. At this point, when moving to a less deformed configuration it can overshoot and induce an aerodynamic load increase, opposite to the original one. This induced vibration causes fatigue and ultimately failure. If the vibration frequency approximates the structural modal frequencies, a growing amplitude motion is generated. Usually, a coupling between a bending mode and a twist mode appears. In both cases, the structural integrity can be seriously compromised [1].

For illustration purposes, let us assume a cantilever wing installed in a wind tunnel, with its root clamped. If one displaces it vertically and then releases it, at low speeds, the oscillation will decrease as the vibration is damped. Increasing the flow speed will result in a damping increase until a certain value. Further speed increment may lead to response that is no longer damped. This is known as the critical flutter speed. A small increment in the flow speed subsequently generates a divergent oscillation [2]. This flutter speed limits the aircrafts flight envelope regarding the velocity not be exceeded. If one considers that this limits the aircraft operation range, one can say that it limits its performance.

The main parameters that determine the flutter speed are related to mass, structure rigidity and modal frequencies and modes. The modal frequencies are directly related to the ratio

between rigidity and mass. Thus, lighter and high stiffness structures with high modal frequencies probably present a high flutter speed. Still, numerical and experimental tests must be performed in order to quantify the flutter speed improvement.

Passive solutions in aeroelastic control include altering structural stiffness and/or mass to postpone the onset of flutter [3]. Also, structures designed with innovative bending-torsion coupling (BTC) behaviour can also postpone or even prevent the aeroelasticity problem. Active solutions have emerged in the past twenty years incorporating smart structures and materials technologies. The scope of application of smart structures and materials solutions is vast and a plethora of innovative solutions have been proposed in the literature in the field of aeronautics:

- Wing shape change, according to flight conditions [4,5];
- In-flight non-destructive evaluation [6];
- Dynamic loads attenuation through active interfaces between aircraft fuselage and wing [7];
- Aeroelastic control of flutter and buffeting [8];
- Exterior and interior noise suppression, without significant weight increase [6];
- Engine intake shape change, according to flight conditions [9];
- Engine thrust direction control [6];
- Blade tip clearance control in reaction engines through shape memory alloys (SMA) application [10];
- Intelligent covering, intended to suppress vibrations [3,11];
- Helicopter rotors active control [12,13].

The focus of this thesis is on the application of active control solutions to aeroelastic control. The pioneering efforts in this area were reported in the fifties [14]. One of the first research efforts on active aeroelastic control was conducted at NASA Langley Research Center's Transonic Dynamics Tunnels [5]. A delta shaped wing carrying leading and trailing edges controls was tested. Gust relief and flutter suppression

techniques were considered successful. In a joint program between the US Air Force, NASA and BOEING, a modern fighter, an F/A-18, was built and successfully tested [15].

The test aircraft has been modified with additional actuators, a split leading edge flap actuation system and thinner wing skins that will allow the outer wing panels to twist up. The traditional wing control surfaces—trailing edge ailerons and the leading and trailing edge flaps—are used to provide the aerodynamic force needed to twist or "warp" the wing.[16].

Similar concepts based on the use of additional surface control actuators have been studied as well [17].

In the last fifteen years, the active solutions have focused on the use of multifunctional materials. In this case, the actuators are part of the structure and directly act on it. Piezoelectric (PZT) actuators and shape memory alloys (SMA) are some of the actuation technologies utilized. The first reported investigations include the Massachusetts Institute of Technology (MIT) study in the nineties [18]. There, Crawley et al [19] used piezoelectric actuators and sensors for the vibration control of a plate representing a wing structure. At the same time, at NASA Langley Research Center, the Smart Wing Program was implemented to conduct realistic and operational level testing of adaptive structures in flight vehicles [20]. There, SMA actuators were used for two different roles: trailing edge shape change to assure a smooth control surface variation and torque tubes to allow wing twisting [4].

More recent studies in active aeroelastic control have also been reported in Europe [21]. More recently, at the Italian Aerospatial Research Centre (CIRA), the use of torque tubes in control surface geometry change has been reported. This resulted in the performance increase with cost reduction [22]. Also, bending and twist control was achieved by changing the position of the flexural axis of the wing at the University of Manchester [23]. At the Portuguese Air Force Aeronautics Laboratory, Suleman et al. have reported several studies on aeroelastic control and flutter alleviation in adaptive flight vehicles [21,

24, 25]. These studies led to two active wing concepts: the active spar and active skin concepts and both wind-tunnel and flight tests were conducted using a Remote Piloted Vehicle (RPV) [26]. A significant increase in the flutter speed and decrease in the amplitude of vibrations was observed. These conclusions were validated for realistic flight conditions [27,28].

1.2 Multifunctional Materials and Actuators

Multifunctional materials are defined as those materials that have intrinsic or extrinsic capabilities to respond to an external stimulus in a useful manner. The external stimulus being sensed could involve a change in a material's environmental condition, such as light, temperature, pressure, humidity, electric field, magnetic field, etc. The response to an environmental change would involve a change in one or more of the material's physical properties; such as, size, shape, color, structure, conductivity, magnetization or polarization, etc. The different actuation technologies are reviewed with respect to the multifunctional materials utilized and the nature of the actuating phenomena for each actuator type.

The shape memory effect occurs in alloys that undergo the thermoelastic martensite transformation. When this deformed material is heated above a critical temperature the material recovers its original pre-deformed shape. The most common commercially available shape memory alloy is Nitinol. This alloy is very ductile and can be deformed easily. In addition, it also has good strength and strain rate, it is corrosion resistant, and it is stable at high temperature[29].

Magnetostrictive materials exhibit a change in dimension when placed in a magnetic field. Terfenol-D is the most popular commercially available magnetostrictive material. Recent research on magnetostrictive materials shows that they provide strokes significantly larger than their electromechanical counterparts however they tend to be difficult to implement in structural systems.[30]

Piezoelectric materials present two distinct characteristics: the 'direct' piezoelectric effect occurs when a piezoelectric material becomes electrically charged when subjected to a mechanical stress. Thus, these devices can be used to detect strain, movement, force, pressure, or vibration by developing appropriate electrical responses, as in the case of force and acoustic sensors. The 'converse' piezoelectric effect occurs when the piezoelectric material becomes strained when placed in an electric field. The ability to induce strain can be used to generate a movement, force, pressure, or vibration through the application of a suitable electric field. The most popular commercial piezoelectric materials are lead zirconate titanate (PZT) and polyvinylidene fluoride (PVDF)[31].

The electrostrictive phenomenon is a nonlinear property which exists in all dielectric materials. When an electric field is applied across an electrostrictive material, the positive and negative ions are displaced and a strain is induced in that material. The resulting strain is proportional to the square of the applied electric field and independent of the applied electric field's polarity. Since the strain is proportional to the square of the electric field, the strain will always be positive. This is analogous with the magnetostrictive behaviour described earlier. In fact, the electrostrictive materials must also have an electric field bias in order to operate bidirectionally (expansion and contraction). The most popular electrostrictive material is lead magnesium niobate (PMN); however, this material is still not widely available on the commercial market. These materials generally offer higher electrically induced strain with lower hysteresis than the piezoelectric materials, however constitutive models for electristrictors are not as mature as models for piezoelectrics due to the nonlinearities [32].

Magneto-rheological and electro-rheological fluids are multiphase materials consisting of a dispersion of polarizable particles in a carrier oil, and they exhibit properties of a typical viscoelastic material. The utilization of electro-rheological materials for vibration damping has been the subject of considerable research since these materials exhibit fast, reversible and controllable changes in behaviour. However, in spite of advances in sensing and controls, fundamental rheological research as applied to vibration damping

has lagged behind. Specifically, essential information in terms of material based structure reliability and controllability is still needed to successfully implement such systems[33,34].

Typically, the performance of an actuator is evaluated in terms of the following characteristics:

- displacement (the ability of the actuator to displace an object; force generation (the amount of force the actuator can produce);
- hysteresis (the degree of reproducibility in positioning operations);
- response time (how quickly an actuator can start the actuation process;
- bandwidth (range of frequencies in which the actuator can operate effectively; temperature range of operation;
- repeatability and precision of the actuator;
- power required to drive the actuator;
- mass of actuator material required for a given displacement;
- cost.

The piezoelectric PZT provides the potential for the greatest force handling capability. PZT also operates with the highest bandwidth of the micro actuators and among the highest displacements. Electrostrictive PMN possesses the lowest hysteresis of any of the actuator materials. However, the temperature operating limits for PMN would require that it be specially insulated. Although PZT is a preferred material for most applications, future commercial applications may favour a direct replacement of PZT with PMN because of its superior hysteresis efficiency.

The shape memory material Nitinol produces the greatest displacements, but the weakest force of the actuators under consideration. This material is very ductile and consequently does not support as much force as the other actuator materials. However, it does give it the advantage of being easily shaped into different actuator geometry. It is less desirable from the point of view of precision and economy of design due to its power consumption,

accuracy and hysteresis characteristics. It can also be observed that Terfenol-D and PZT compare very closely in these general characteristics. For deformation of thin structural elements, the most widely used multifunctional materials to date have been piezoelectric actuators. Piezoelectrics have higher bandwidths than are possible in shape memory alloys, they are more compact than magnetostrictive devices and they are bidirectional by nature unlike electrostrictive materials.

1.3 Bending-Torsion Coupling

Piezoelectric actuators and sensors are nowadays reliable for industrial applications. They have the advantage of their application being easily achieved, independently of the base material. For instance, they can be bonded (surface glued or embedded) to metal, carbon, composite, etc. The coupling between the actuator and base structure can be easily enhanced in composite structures if one uses a misaligned layer stacking. If a flat beam is considered, the misalignment is the fibre angle deviation from the length direction. The misalignment can vary from 0 degrees (aligned) to 90 degrees (perpendicular alignment). A structure built with this type of internal layout when loaded vertically will deform vertically and twist. The same effect can be attained if a torsion moment is applied. An inherent consequence is that the vertical displacement and torsion are no longer linear with respect to the specific load applied.

Several solutions have already been proposed to attain this kind of coupling. Examples of it are the D-Spars [35] and active systems to control the twist stiffness [36]. These concepts have already been tested on real applications. The method intended to be explored in this thesis is a different approach, that has not been yet proven in wind-tunnel and flight tests.

The bending-torsion coupling (BTC) is assumed as a ratio between the torsion and the vertical displacement suffered by a beam. As the misalignment increases, from 0 to 45 degrees, the vertical stiffness is penalized and the torsion stiffness increases. A typical BTC evolution with respect to the misalignment imposed is given in Figure 1.1 [37]. It

can be observed that the evolution is clearly nonlinear. Early studies on this field were carried out by Garfinkle and Pastore [37]. They analyzed the passive and augmented active behaviour of structures exhibiting BTC as shown in Figure 1.2 [38]:

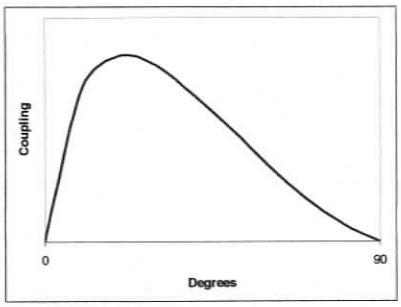

Figure 1.1 BTC evolution

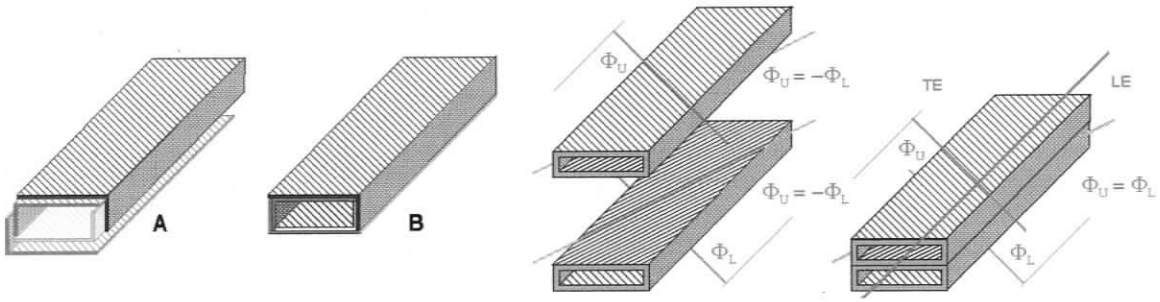

Without midwall (A) With midwall (B)

Figure 1.2 Beam layouts [37]

The layout on the left presented a problem related to the obviously fragile corners, due to the fact of presenting a discontinuity on the fibres. Therefore, another solution was proposed [39, 40], resulting in the second layout presented (B). Here, the span wise direction is referenced and the TE and LE position is depicted.

It was further analyzed and exhibited a pronounced BTC, which was higher for misalignments around 17 degrees [41]. Furthermore, the damping on a conventional wing depends on its internal structure. A wing with a misaligned spar has an added damping factor due to its convergent behaviour. The difference can be seen in Figure 1.3.

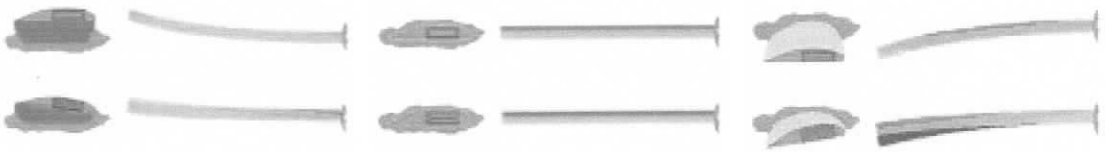

Figure 1.3 BT spar movement [37]

The aerodynamic loads on the BT coupling wing work as a restoring force. Compared to a conventional wing, lighter and cheaper wings can be built using the proposed techniques [42]. This idea was put in to practice on the X-20 experimental aircraft presented in Figure 1.4. Patches were laid, overlapping on the wing edge thus suppressing the unstable behaviour on roll manoeuvres due to the swept-forward wings.

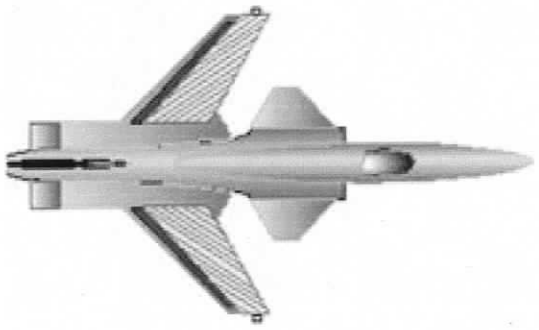

Figure 1.4 X-20 Wing's fibre layout [37]

The BTC solutions are also aimed at vibration reduction and control. For certain fibre angles and multi cellular cross section configurations, certain types and level of coupling can be achieved, such that it can be utilized to counteract aeroelastic deformations resulting in flutter and divergence.

1.4 Thesis Layout

The thesis structure reproduces the natural sequence of the project execution. Chapter 1 presents the background and motivation, a brief literature review and the proposed design principles. Chapter 2 details the proposed spar concept and the manufacturing process. Also, an optimization problem is formulated and solved with reference to the constraints and the design objective function. Ground vibration tests were carried out and the results are compared with computational predictions using ANSYS. This comparison allows the refinement of some parameters and realizing some manufacturing issues. A first assessment of the active system implementation performance was also conducted.

Chapter 3 discusses the results attained with a wing built using the spar with bending-torsion properties. Some design considerations are mentioned in order to justify the wings internal structure, which truly determines the placement of the active elements. Wind tunnel test results are shown and compared with the ones obtained using an ANSYS model. The experimental results are in good agreement with the computational model. Further wind tunnel test related to structural damping and vertical displacement determination at several speeds were necessary to quantify the benefits of the proposed wing design. During the project and at this point it was decided to manufacture a spar with no misalignment for comparison with the baseline model. This exercise allowed quantification of the improvement that result solely from fibre misalignment, i.e., without considering the active system. It was shown that fibre misalignment contributes to improving the wing response and further improvements were observed when augmenting the vibration suppression using the active elements.

Chapter 4 presents the results of the active spar in real flight test conditions. The wing was modified to fit in to the existing flight demonstration platform. The wing installation, all necessary systems assembly and electronics on a remotely piloted flight vehicle poses are explained and some flight test observations are given.

Chapter 5 summarizes all the major achievements throughout all the project. The final contributions to practical applications and active systems state of the art are mentioned. Finally, several future work issues are mentioned. Some are related to necessary improvements to the presented systems, and the remaining are related to future fields of application.

CHAPTER 2

MULTI-CELL CROSS SECTION SPARS

In this chapter, the design and optimization of a multi-cell cross section spar is presented with the objective of implementing a bending-torsion coupling property to counteract the aeroelastic response of the wing. However, when designing a multi-cell configuration, inner mid-wall issues must be addressed as these will have a small contribution to the inertial moment, i.e., flexure and torsion resistance, compared to the outer walls, while contributing the same amount to the total weight of the spar. This of course is a disadvantage of this configuration, but one must also take into consideration that the inner walls will significantly contribute to the buckling resistance of the spar. No skin buckling issues are brought up since the skin is made of a thin film. Also, if multi-cell cross section spars are embedded with active materials, the aeroelastic suppression can be further enhanced.

The projected milestone in this chapter is to design, optimize, manufacture and test a continuous filament multi-cell cross section composite spar with bending-torsion coupling and with embedded piezoelectric actuators. Static loading and dynamic tests, with passive and active wing spars were performed, where deformations, rotations (coupling), natural frequencies and active behaviour – vibration damping, frequency change and induced BTC performance – were quantified. At the end of this effort, an active multi-cell cross section spar was implemented in a real wing to be tested in a wind tunnel and flight test conditions.

2.1 Design Considerations

There are advantages that arise from the use of a wing spar with a multi-cell cross section, due to the fibre misalignment. This property consists of structurally coupling the bending and torsion response of the spar and can be used to counteract the aerodynamically

induced bending/torsion aeroelastic coupling. The static aerodynamically imposed deformations on the wing structure, opposition and reduction of the dynamic response, especially the unstable behaviour such as flutter and divergence (or at least delay it), are some of the possible benefits arising from the concept presented. This advantageous BTC concept is explored using a multi-cell cross section spar in conjunction with orthotropic materials, with a preferable direction on a conventional spanwise straight spar with rectangular plan form.

Consider a bar made of unidirectional carbon fibre composite. The fibres are not aligned spanwise (preferable direction), but make an angle θ with the spanwise direction. When loaded in traction or compression, or bending, the coupling of fibre force into torsional direction will result in the desired BTC effect.

When considering a spar with a hollow rectangular single cell cross section, attention has to be paid to the construction of such a spar with misalignment of the composite fibres. In order to avoid fragile and critical bonding areas, or heavier and over dimensioned fibre superpositioning, composite fibres must be wrapped around the spar in the chordwise direction and in an evolving fashion (in a spiral) in the spanwise direction. Thus, in the upper surface of the spar, fibres are oriented in a symmetrical manner, with respect to the fibres on the lower surface of the spar. When bending the spar upwards, about the vertical plane, the upper fibres compress and the lower fibres extend, due to their symmetrical orientation torsion is induced.

Furthermore, if a constant wall thickness and a rectangular exterior cross section are considered, the only way to achieve bending/torsion coupling, corresponding to obtaining the same direction on the fibres of the upper and lower walls of the spar, is that the spar must have at least two cells vertically (i.e. in the thickness-wise direction of the airfoil).

The construction of this type of spar consists essentially of several separate spars built and glued together. Each spar has a cross section that is a portion of the whole spar cross section. These spars are joined during the fabrication and cured in compression so that

they act as a unique multi-cell cross section spar, without weak bonding areas. The resulting middle section walls will have a thickness that is the double of the other spar walls. Despite their lower contribution to the inertial moment, they help avoid buckling problems by increasing the structural rigidity.

By orienting the upper and lower wall fibres from trailing edge to leading edge, from root to wing tip as shown in Figure 2.1 (note the TE position), the spar twists in a manner that the angle of attack is decreased (leading edge down) when it bends upwards (p.10). Thus, with the proposed fibre orientation, a desirable behaviour is attained as it counteracts the unstable dynamical behaviour in flutter. The effect of fibre misalignment is considered as a passive property of the spar. This characteristic can be enhanced by embedding or gluing piezoelectric actuators on the upper and lower multi cell spar walls combined with an active control system.

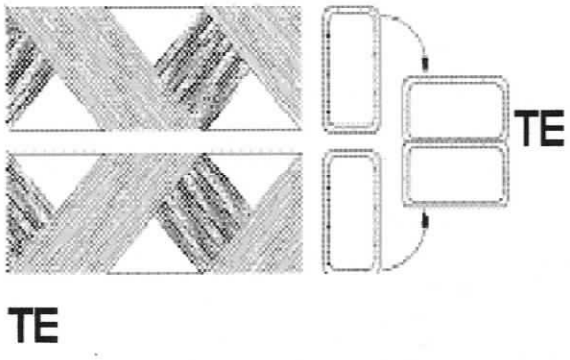

Figure 2.1 Semi-spars and fibre layout

2.2 Optimization Problem

In order to design a multi-cell cross section spar with fibre misalignment, there are several aspects to take in consideration such as:

- Number of cells;
- If the cells are joined or separated;

- Composite fibre orientation;
- Cross section dimensions of the multi cell spar (directly related to weight, rigidity, available volume and actuator placement).

Some of these aspects can be simplified if one considers the fabrication issues and constraints. The number of cells must be an even number. Only stacking up pairs of cells one can achieve the same misalignment on the top and bottom final spar surfaces. So, only two cells are considered, as it would be very difficult to fabricate a spar with more cross-sectional cells and it would further penalize the weight of the structure. Thus, a two-cell spar model is deemed to be an appropriate configuration for this application. However, the determination of the optimal fibre misalignment with respect to the spanwise direction and the size of the cross section dimensions require design optimization.

In order to formulate the optimization problem, an objective function, a set of design variables and constraints are required. The design variables are directly related to the spar design, namely its dimensions and fibre orientation and they may be governed by geometrical constraints. The state variables are related to the spar performance (levels of stress and strain, modal frequencies, etc.) and weight. These state variables play an important role in the objective function definition and they also have constraints.

The objective function is defined in a way that translates the design objectives, into a numerical expression. The primary consideration in any aircraft structure is its mass, it is desired to be as light as possible. The maximum bending-torsion characteristic is another design objective. This coupling is calculated based on the rotation about the spanwise direction (torsion) and the displacement along the spanwise direction (bending). This property encompasses several behaviours because it depends on the structure rigidity. Finally, the modal frequencies are also selected because the modal response of a wing is important as flutter results from coalescence of bending and torsional modes of vibration. The final objective is to find a spar that exhibits a desired BTC, which has low mass and a

high first modal frequency. Thus, the optimization problem is formulated based on the set of design variables:

- Spar width (x_1);
- Spar wall thickness (x_2);
- Fibre misalignment with the spanwise direction (x_3)

As there is no explicit objective function is this case, a relationship between state variables can be defined. An ideal spar has low mass (m), high 1st modal frequency (f_1) and high BTC. Thus, the following objective function is defined in Equation (2.1).

$$Objective \quad Function\left(x_1, x_2, x_3\right) = \frac{m^3}{BTC \times f_1} \tag{2.1}$$

Each of the state variables has to be weighted in such way that they represent their relative importance in the design optimization process. All state variables were also adimensionalized by a specific reference value. This way, all of them have the same order.

The geometric constraints are based on the available volume and construction limitations:

- Span - 1m (determined by the wind tunnel section available);
- Height – 0.035m (determined by the airfoil maximum thickness, this way the cross section inertia moment is the maximum);
- Width - min 0.045m max 0.055m (determined by the airfoil) ;
- Wall thickness – min 0.001m max 0.002m (determined by the manufacturing process limitations);
- Fibre orientation – min 0° max 45°. (determined by the useful range of misalignments)

The spar must be able to sustain a lift of 5 *kg* on a 2.5*g* manoeuvre, plus a safety factor of 1.5. These data is provided by the Remote Piloted Vehicle requirements. This corresponds to a maximum upward force of 180 *N*. This leads to the material (carbon fibre) limits:

- Maximum normal stress:
  - Along Fibre 1.5 *GPa*;
  - Cross Fibre 0.3 *GPa*;
- Maximum compression stress 1.3 *GPa*;
- Maximum shear stress 0.05 *GPa*.

The finite element software ANSYS is used to model the spar. Two optimization approaches are presented. The first one is based on one of the optimization tools provided in ANSYS, the other one is based on a global optimization approach, namely metamodeling. A metamodel is a representation of the true model which can be obtained and minimized, using conventional optimization tools. This type of approach offers better assurance concerning locating the global minima. A technique was developed to be used in this specific design optimization case.

2.3 Finite Element Model

An ANSYS model was created based on generic design variables. The material used is carbon fibre, so its mechanical characteristics were introduced. A Shell-91 element was chosen and a mapped mesh was selected, producing a finite element model with 2500 elements. The spar is clamped at the root and a distributed pressure is applied, simulating the maximum design load. A static analysis was performed and a modal analysis was carried out to calculate the 1st natural frequency (on this one, no load is applied).

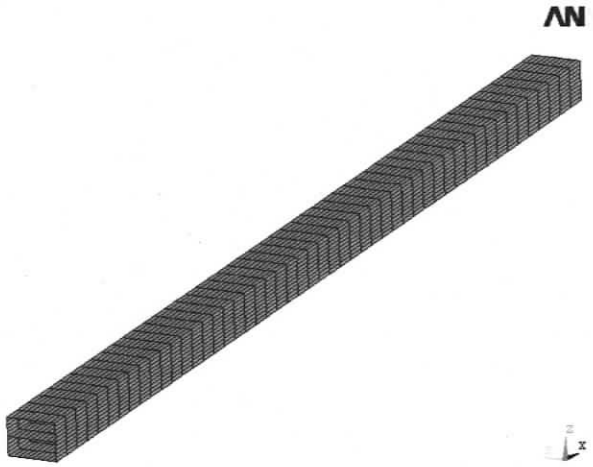

Figure 2.2 ANSYS spar finite element model

Several tests using different sets of design variables were done to study the model behaviour. Analyzing the results, it was possible to conclude that the structural limits were never attained, so all possible set of design variables result in a safe structure. Consequently, the related constraints were removed as they do not affect the solution. The subproblem approximation method was chosen in ANSYS to perform the optimization. It is a zero-order method in that it requires only the values of the dependent variables, and not their derivatives. There are two concepts that play a key role in the subproblem approximation method: the use of approximations for the objective function and state variables, and the conversion of the constrained optimization problem to an unconstrained problem.

In more detail, the dependent variables are first replaced with approximations by means of least squares fitting. Using penalty functions, the constrained minimization problem is converted to an unconstrained problem. Minimization is then performed every iteration on the approximated, penalized function (subproblem) until convergence is achieved or termination is pointed. Each iteration represents one complete analysis loop. Since the method relies on approximation of the objective function and each state variable, a certain amount of data in the form of design sets is needed. The method itself will generate design sets at random, unless the user determines it. [43].

The ANSYS iterations and the results are shown in Figures 2.3 and 2.4. Also, the optimal design variables solutions are tabulated in Table 2.1. It is noted that the optimal solution reveals that the optimal thickness value is 4.51 cm and the number of layers is 4.

Analysing the iteration evolutions, one can conclude that the objective function is very sensitive to the thickness, and less sensitive to the width and misalignment. The second result is not obvious because the mass depends directly on it. Higher widths also produce more twist. What happens is that, despite higher widths penalize the mass, they favour the BTC. That's why the function objective is not very sensitive to this fact.

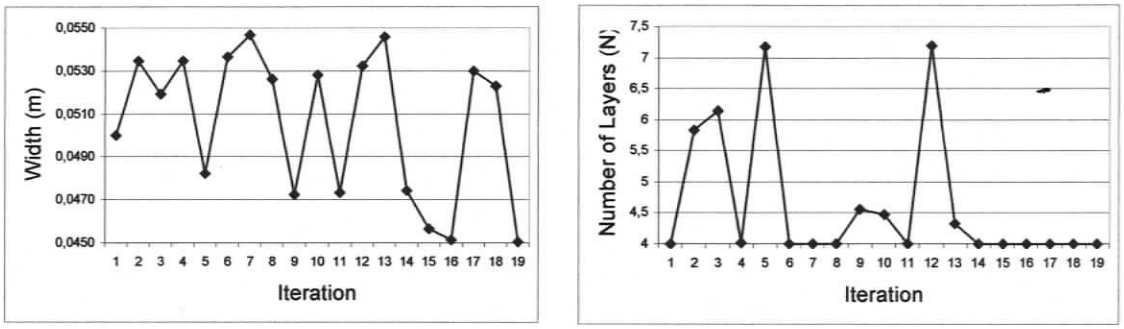

Figure 2.3 ANSYS Results: Width and Misalignment Values Evolutions

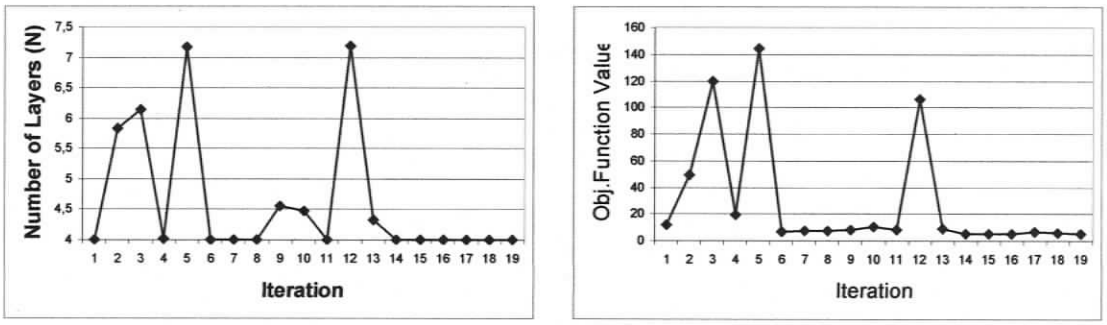

Figure 2.4 ANSYS results: number of layers and objective function values solution evolution.

Table 2.1 ANSYS optimum design variables values

Iterations/Function Evals	Width (m)	Misalignment (degrees)	N. Layers (Thickness)	Obj. Function Value
19/19	4.51e-02	6.83	4.0	5.00

2.3.1 Metamodeling Approach

A metamodeling approach was chosen as an alternate optimization technique for this problem. In this method, at each iteration, a fixed number of 27 points (a point is defined by a determined x_1, x_2 and x_3) based on D-Optimal design are chosen [44]. Using this design and considering the feasible domain, all 27 design variable set are symmetrically distributed along the domain's border. This way, the function to be fitted has equal information about every domain regions.

The objective function for each point is calculated using ANSYS. Next, a quadratic function (includes interactions and squared terms) is fitted. The function is the form given in Equation (2.2) and x_1, x_2 and x_3 are the same design variables used on the objective function definition (p.17):

$$f(x_1,x_2,x_3) = \beta_0 + \beta_1 x_1 + \beta_2 x_2 + \beta_3 x_3 + \beta_4 x_1 x_2 + \beta_5 x_1 x_3 + \beta_6 x_2 x_3 + \beta_7 x_1^2 + \beta_8 x_2^2 + \beta_9 x_3^2 \tag{2.2}$$

The D-Optimal design range is decreased by a certain amount after each iteration according to Equation (2.3):

$$RangeDecrease = (DecreaseFactor)^{IterationNumber-1},\ 0 < DecreaseFactor < 1 \tag{2.3}$$

The process continues until convergence is attained. In the case presented, the process was stopped manually. In the case presented, when the misalignment change was inferior to 0.01 degrees and the change between the estimated value and true value was inferior to 0.4%, the optimization process was terminated. The algorithm follows the scheme presented in Figure 2.5. The design iterations and results are shown in Figures 2.6 – 2.8. Finally, the optimal design variables are tabulated in Table 2.2.

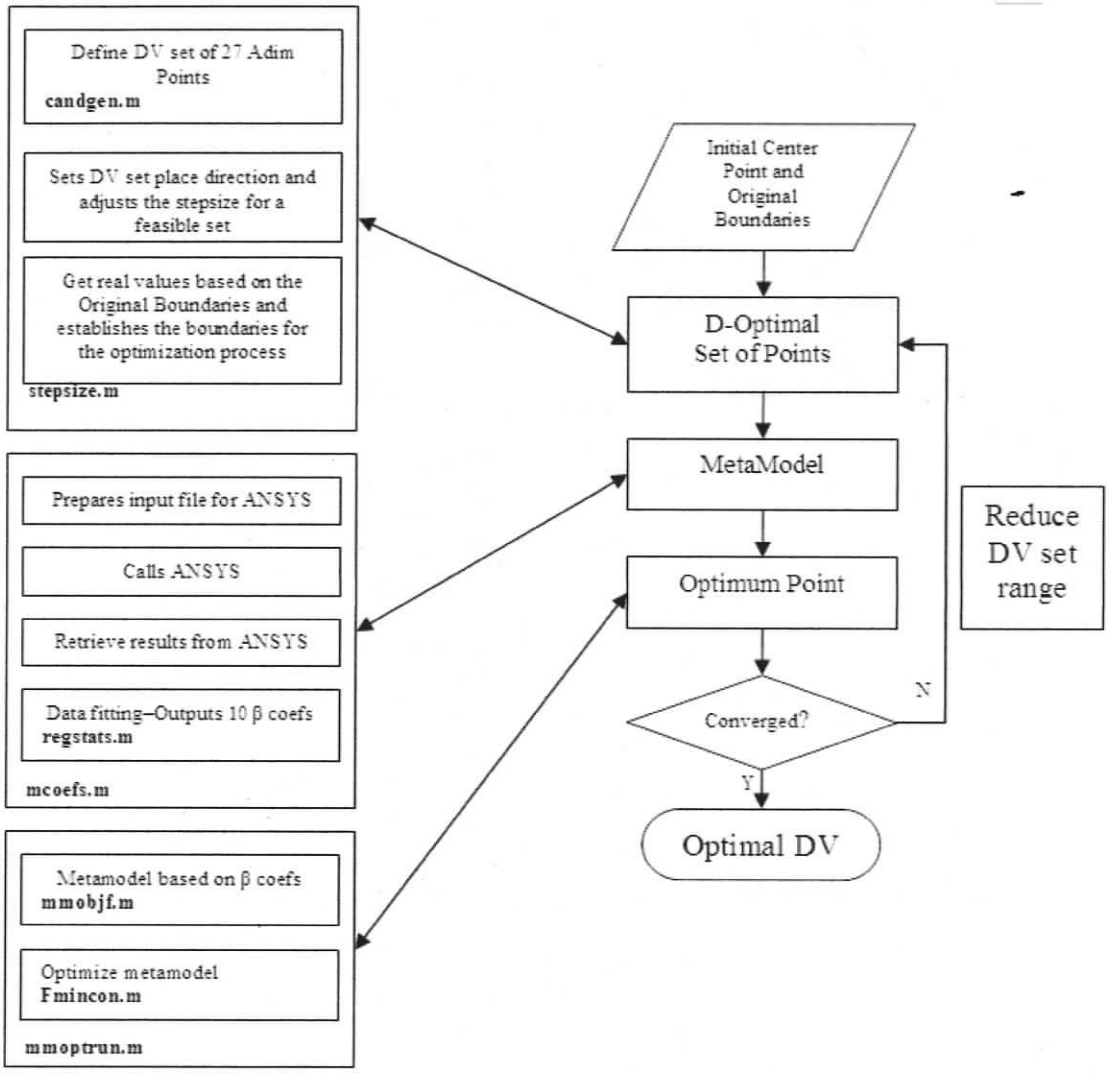

Figure 2.5 Metamodeling flowchart

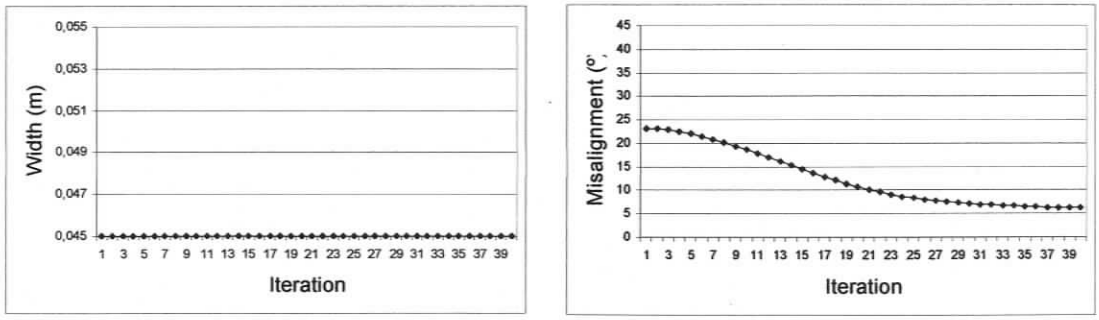

Figure 2.6 Metamodeling results: width and misalignment values iteration history.

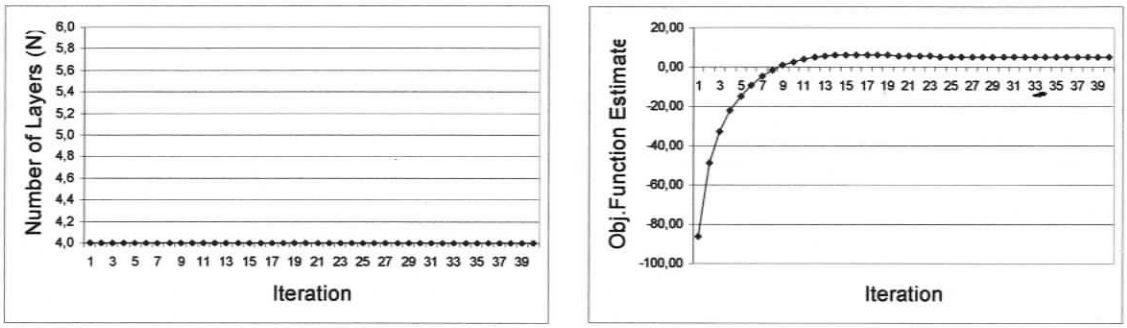

Figure 2.7 Metamodeling results: number of layers and objective function iteration history

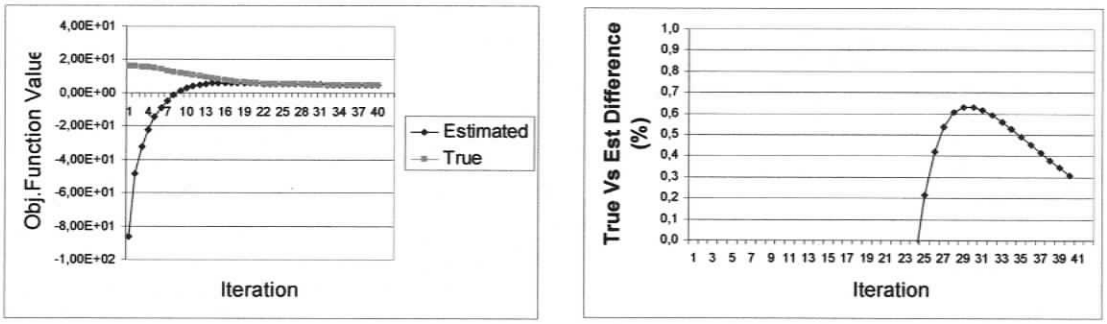

Figure 2.8 Metamodeling results: objective function convergence history

Table 2.2 Metamodeling Optimum Design Variables Values

Iterations/Function Evaluations	Width (m)	Misalignment (Degrees)	N. Layers (Thickness)	Obj. Function Value
40/1080	0.0450	6.23	4.00	4.92
ANSYS (True Value)	0.0450	6.23	4.00	4.90
Comparison				**+0.3%**

Analysing the design variables evolution during the iterative process, right after the 1st iteration only the misalignment is considered for the optimization because the two other variables remain constant at the minimum level. This is a direct result of using such high weight for the state variable mass on the objective function. In fact, using the minimum values allowed for thickness and width, the minimum mass is attained.

Summarizing, both approaches achieved approximately the same result. Although the metamodeling approach resulted in a lower value for the objective function, the computational effort was larger than ANSYS. Each function evaluation takes about one minute. Since metamodeling evaluates the objective function 27 times for each iteration, it took approximately 18 hours to achieve the result presented. ANSYS only took 19 minutes to achieve a similar result. It can also be concluded that the metamodel fairly approximates the real objective function at the optimum point, as expected. A difference of 0.3% as found.

2.4 Fabrication Process Issues

Manufacturing issues are important in the design process when experimental testing is the final objective. For example, consider the accuracy that is achievable when aiming for a constant spanwise fibre orientation angle. A sensitivity analysis was conducted to determine the influence of the error that can exist when orienting the fibres. To this end, the spar width and number of layers were assumed constant and optimal. Several models

were run between 0 and 14 degrees to access the objective function sensitivity to this parameter and the results are shown in Figure 2.9.

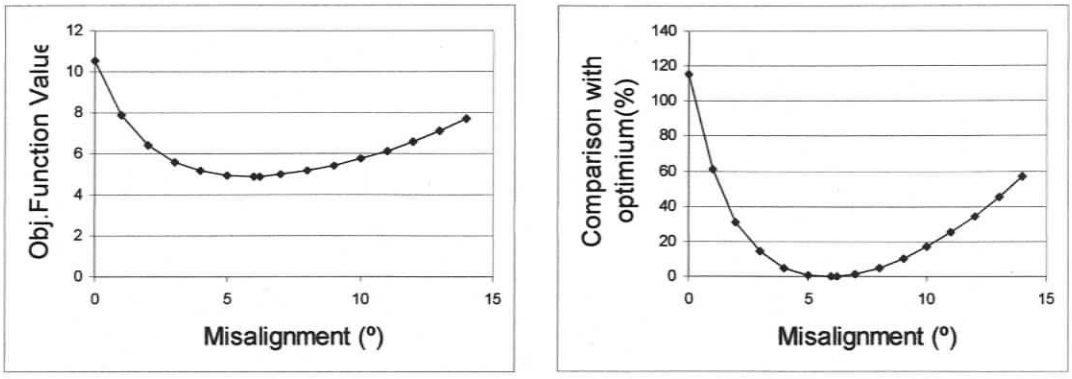

Figure 2.9 Objective function sensitivity analysis

It can be observed that for angles smaller than 6.22 degrees the objective function sensitivity is higher for fibre orientation values inferior to the optimum found. Bearing in mind that the BTC plays an important role in the design, it was decided to use a higher angle for the fibre orientation, in order to minimize the effect of fibre angle on the BTC property. This angle was set at 10 degrees.

2.5 Modal Analysis

For the selected 10-degree angle for the fibre orientation, the computational results obtained using ANSYS are shown in Figures 2.10 - 2.12 where the first five natural modes and frequencies are depicted. The natural frequencies and the mode shapes are described in Table 2.3.

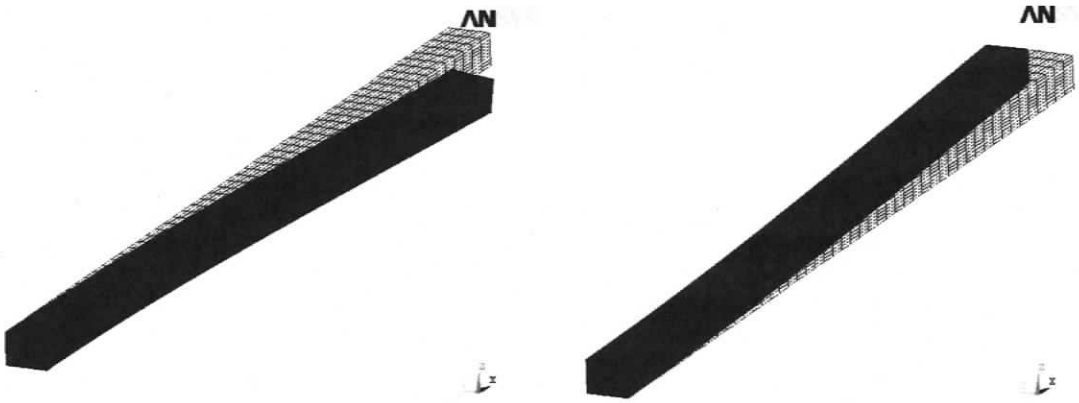

(A) (B)

Figure 2.10 1st vertical (A) and horizontal (B) bending modes

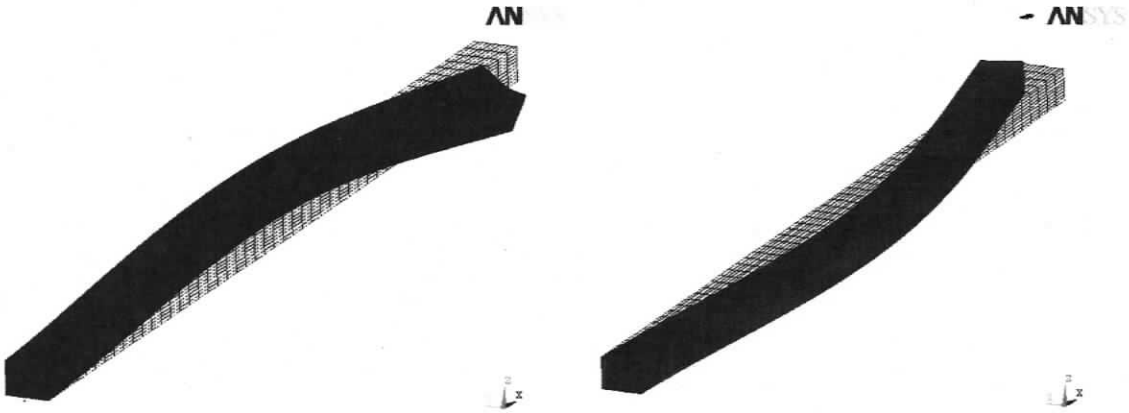

(A) (B)

Figure 2.11 2nd vertical (A) and horizontal (B) bending modes

Figure 2.12 2nd horizontal bending (A) and 1st torsion modes (B)

Table 2.3 The first five natural frequencies and mode characterization.

Freq (Hz)	Mode Description
44.79	1st Vertical bending mode
65.40	1st Horizontal bending mode
253.9	2nd Vertical bending mode (showing a significant amount of flexure - torsion coupling also)
399.1	2nd Horizontal bending mode
432.6	1st Torsion Mode

Table 2.4 ANSYS Spar Model Maximum Load Response

Mass (kg)	Vertical Displ.(m)	Rot. X (degrees)	Rot. Y (degrees)	Coupling
0.387	0.0089	-0.0252	-0.0115	2.185

Thus far only the passive model results have been presented. As a preliminary assessment of the active system, the spar was modelled with actuators using ANSYS. In this model, actuators were positioned near the root on the upper and lower spar surfaces and were modeled by applying displacements on the nodes on the actuation region. Actuator dimensions and outputs were simulated using the Quickpack QP40W actuator information, for an average output. The actuation displacements transmitted to the structure were applied taking into account an estimated damping and transmissibility factor. Figure 2.13 and Table 2.5 show the results of a static analysis.

Figure 2.13 ANSYS active spar model showing the maximum load response

Table 2.5 ANSYS passive and active spar response

	Passive	**Active**
Maximum Displacement (m)	0.008931	0.00018324
Coupling	2.18	2.8

The results show a significant performance improvement. For the same applied bending load, the bending deformation decreases significantly and the desired coupling effect is augmented. This finding shows that a significant improvement in flutter delay can be achieved using active multi-cell spars. This analysis also allowed determination of the best locations to place both actuators and sensors. The actuator and sensor placement is further explained in the active tests section.

2.6 Experimental Models

For the construction of the multi cell spars, inner foam moulds were formed for each of the two cell sections. Carbon unidirectional tapes were wrapped around those moulds, using the filament winding technique. The 10-degree angle with relation to the span direction was maintained. After the two single cell section spars were manufactured, they were positioned one in the top of the other, inside a wood and aluminium compressive mould. This mould is a completely closed section, just open at its root and tip. Thus the multi-cell section spar is formed since the two small single cell spars are in compression,

and the exterior walls are compressed between the inner and outer moulds and the inner mid walls are compressed to each other between the two single section inner moulds. Since the resin is still wet, that is, the curing process was not yet started the mid walls of the small single section spars were perfectly bonded to each other, i.e., they form a perfectly single carbon multi-ply wall, with double the thickness and carbon plies as the other exterior walls. After compression is applied to the exterior mould, the set of moulds and the contained spar are put inside the oven to perform the process of curing of the carbon composite laminates. The spar is separated from the exterior mould by a plastic wrap to facilitate de-moulding of the spar. The inner moulds were removed mechanically.

When the spars walls were in compression between the inner and outer moulds, and the outer mould was opened at its root and tip, excessive resin was spilled out by the root and tip open sections of the exterior mould.

It is noteworthy to point our that several unsuccessful tries were performed using the vacuum bag technique. Using this method the exterior spar shape attained was extensively deformed.

2.7 Passive Control Tests

2.7.1 Static Tests

To perform the static tests the spar was clamped at its root. Several loads at different spanwise positions were tested and the results were compared with the computational simulations using ANSYS. Two types of tests were executed:

- Concentrated, increasing loads on half span to confirm the expected linear behaviour between bending deformation with respect to the applied load and assess the BTC. These tests also had the objective to validate material properties, the fabricated spars and computational models
- Spanwise distributed loads to simulate the worst load case that can be found in the flight demonstrator vehicle flight envelope, including a safety factor.

When comparing displacements obtained from the above tests with the computational ones, unexpected excessive displacements were observed in the real tests. Several tests were executed with different load cases. Since a linear behaviour between displacement and applied load was always observed, it was concluded that the Young Modulus (E_x), along fibre length, was lower than the theoretical one, used on numerical models.

The theoretical typical value for E_x for unidirectional pre-preg ply, on dry and room temperature conditions and for a fibre volume of 60% is 135 *GPa*. To evaluate the real specimen E_x, a simple 2D beam analysis was performed. Adjusting the value for E_x according to the displacements observed, a significantly smaller value of approximately 35 *GPa*, was found. Using this new value for E_x on the numerical models, immediately a match between experimental and numerical tests was observed, for spar tip vertical load solicitations.

The E_x difference initially observed is due to the fibre volume obtained during the fabrication process. According to the manufacturing process described earlier, internal and external spar shapes must be guaranteed. This is unfeasible using the vacuum bag method, because an external mould, in addition to the internal one, must be used. Therefore, insufficient resin is retrieved from the fibre/resin mixture just by the compression applied to the external mould. This decreases the relative fibre volume, which implies a fibre composite E_x reduction. The E_x obtained corresponds to the maximum compression possible. The remaining E_y and E_z were also proportionally corrected. The results obtained for both the real spar and the corrected ANSYS models for the first type of tests, are shown in Table 2.6 and Figure 2.14.

Table 2.6 Experimental and ANSYS Vertical Displacements

Load (N)	Experimental (mm)	ANSYS (mm)
5.68	1	0.52
12.82	1.5	1.18
18.97	2	1.75
38.11	2.5	3.52
57.08	4.9	5.27
77.08	7.5	7.17
111.11	10.5	10.27
140.29	14.5	12.96
165.86	16.5	15.32
190.62	19	17.61
206.21	22.5	19.05

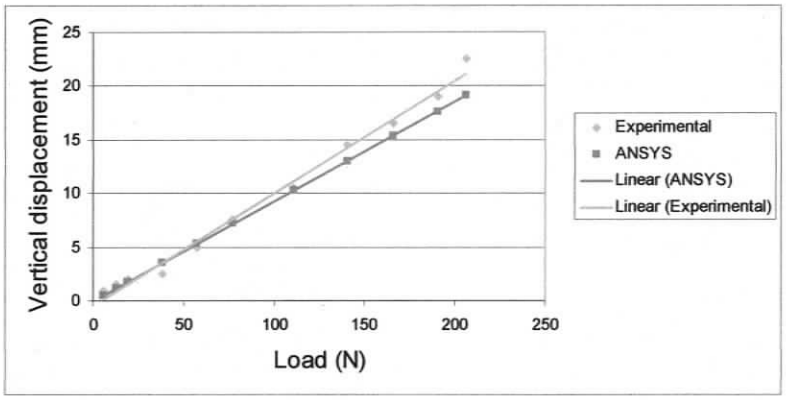

Figure 2.14 Experimental and ANSYS Vertical Displacements

As expected, both numerical and experimental results provide a linear relationship between the load applied and the displacement attained. The trend lines shown tend to slightly grow apart as the weight is increased. In fact it was difficult to get an accurate vertical displacement measurement because the twisting grows higher as the load increases. Despite the difference stated for higher load cases, the loads tests between 0 and 180 N are much similar, and this is the operation range.

To conclude the static tests, the worst load case simulation test was performed. Despite the E_x reduction, the spar was able to sustain the applied load without any permanent deformation, i.e., it never exceeded the yield limit. The distributed load was simulated by applying several different weights placed over a ruler as shown in Figure 2.15 (the weight of the ruler was also considered). The load distribution was done assuring that both shear and moment at the spar root were the same as for the ANSYS models. The ruler was placed on the most forward half spar chord, in order to simulate the aerodynamic pitch moment (the same condition was considered in ANSYS models). The results are shown in Table 2.7 and a good correlation was obtained between the experimental and computational results.

Figure 2.15 Experimental Setup

Table 2.7 Maximum vertical displacement results

	Max Vertical Displacement
Experimental	19.2 mm
ANSYS	17.89 mm
Difference	7.3%

2.7.2 Dynamic Tests

Following the static tests, the dynamic behaviour of the spar was investigated. The OROS system was used to measure the first five natural frequencies (p.27). This system consists of an accelerometer connected to the spar tip and an Fast Fourier Transform (FFT) analysis algorithm. Random vibration inputs were imposed on the spar and OROS, using the sensed vibration at the accelerometer, to calculate the desired natural frequencies. These random vibrations were inflicted by hitting the structure with a special rubber hammer. The results obtained experimentally and the comparison with the computational simulations are shown in Table 2.8. The results are also shown graphically in Figure 2.16 and the ANSYS prediction fairly approximates the real tests results. This also validates the E_x correction.

Table 2.8 OROS and ANSYS modal frequencies

Frequency No.	Oros (Hz)	ANSYS (Hz)	Diff. (%)
1	29.2	28.8	-1.4
2	41.0	41.0	0.0
3	177.0	172.4	-2.7
4	254.0	247.3	-2.7
5	329.0	343.9	4.3

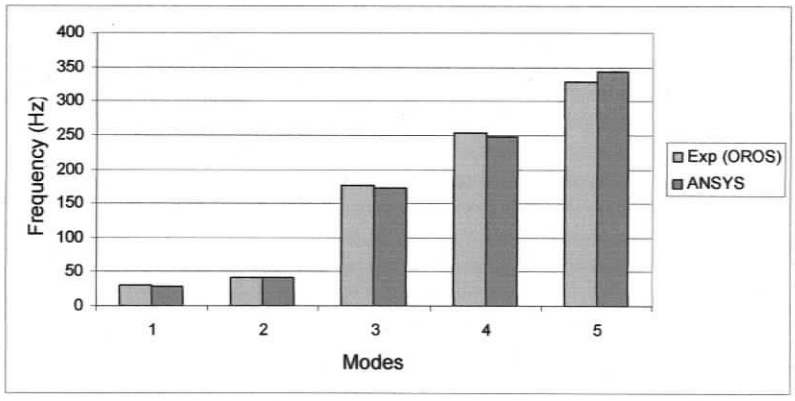

Figure 2.16 OROS and ANSYS modal frequencies

2.8 Active Control Tests

Two pairs of actuators were installed on the spar. The first pair was positioned on the upper and lower spar surfaces, just 4cm outboard of the root. Similarly, the second pair was positioned just outboard of the mid span location. These locations were chosen because they experience the highest deformations (static and dynamic response).

The actuators installed on the upper spar are actuated in the same manner, extending or compressing. Simultaneously, the lower surface actuators are both actuated also in the same manner but inverse with reference to the upper ones, i.e., compressing and extending respectively. With this behaviour, upwards or downwards bending motions can be created.

Also, one pair of PZT sensors was positioned on the upper and lower spar surfaces, just inboard of the mid span position and a second pair just inboard of the spar tip. Actuators are connected to an amplifier, which input signal (coming from the controller) is filtered by a signal conditioning module. This signal is generated by the DSPACE module, according to the control laws and inputs uploaded on it. On these specific tests, the DSPACE module is connected to a laptop in order to change inputs and output in real time.

Figure 2.17 shows the SIMULINK program uploaded to the DSPACE microcomputer. Essentially, it allows implementing an automatic feedback loop, which reads the sensor signal and outputs signals to the actuators. This is the mode used on true active tests. It also has a manual input configuration, which allows testing the instrumentation and performing quasi-static tests.

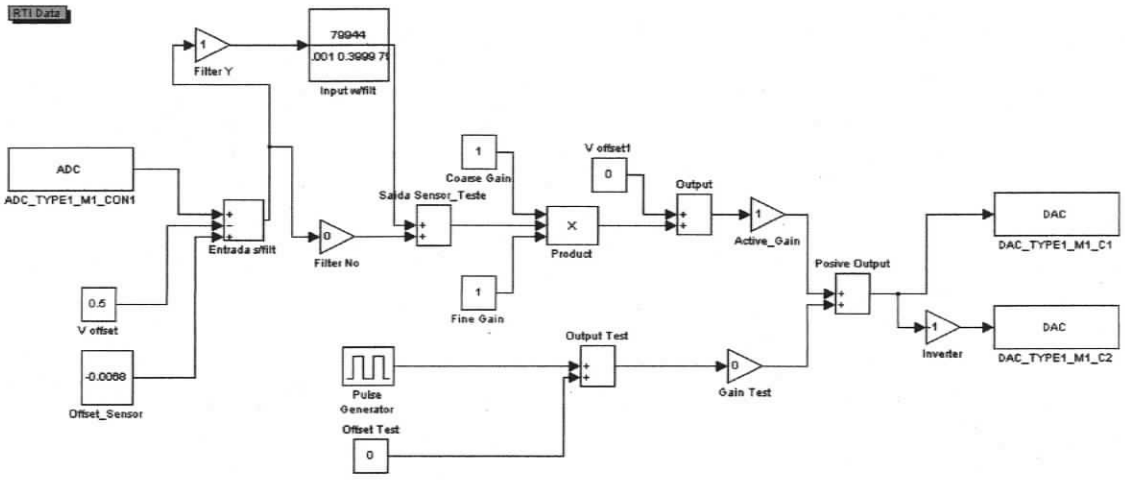

Figure 2.17 SIMULINK control law model

2.8.1 Quasi-static Tests

Initially, the active behaviour was studied on an unloaded clamped spar. The tip vertical displacement was measured by supplying the maximum actuation voltage to the actuators. Since actuators only perform above 1Hz excitation frequency, a sinusoidal voltage of the lowest frequency possible (1Hz) was input. This is the reason the tests are classified as quasi-static. A maximum tip vertical displacement of 0.5 *mm* was obtained, either on upwards or downwards bending motions. This result was successfully compared with computational analysis. It was also observed that the total deflection and input voltage corresponds to a total actuator extension or compression strain of 100 $\mu\varepsilon$. With strains higher than the value presented, the actuators will saturate and the spar will only react in only one direction, opposite of the applied load.

To assess the actuation capability under applied load, several tests were executed, varying concentrated applied weights. The results showed that the active spar can recover approximately 0.5 *mm* of the vertical tip displacement. This is an expected behaviour considering the actuators saturation, as mentioned above.

2.8.2 Dynamic Tests

The dynamic tests were performed using the same apparatus, i.e., the same active spar, with the same dimensions, configuration and fabrication methods. One of the midspan PZT sensors is connected to the signal conditioning module, which makes it compatible to the DSPACE unit input signal requirements. On the controller unit, a previously uploaded Simulink MATLAB code performs filtering and applies a gain to the input signal. After this stage, the conditioned output is sent to the actuators. This way the actuators will oppose the sensed movement.

In fact, PZT sensors sense strains. Since they are glued to the spar, whenever the spar is bent, they will sense compressive/extensive strains. A proportional signal will be output which also corresponds to the change of the spar tip vertical position (directly related to the strain sensed).

Several different simple control laws were studied: proportional, integral and derivative methods. A proportional law is quite simple and thus more reliable, fast in response and easy to implement. It does not compute the true position of the spar but the sensors signals provide a good feed for the system by themselves. The other methods are very complex and require a high calibration effort, which is time consuming. A proportional feedback control law was chosen, as shown in Figure 2.18. Using this method, whenever the PZT sensors senses a change, a counter acting response will be generated by the PZT actuators. For vibration reduction one of the midspan PZT sensors is used. For example, if the chosen is the spars top surface one, whenever the spar is bent up it will sense a compression. Due to this, it will output a signal that will command all four PZT actuators to counteract. The ones on the top of the spar will extend and the ones on the bottom will contract. This way, a decrease in the bending amplitude is attained.

These tests were performed with the help of an external vibration exciter connected to the spar, but mainly by statically deforming the spar by applying the maximum distributed load to it and then suddenly releasing the loads and letting the spar vibrate in natural free

damped vibration. This was done to the spar with the active system off and on. The results are summarized in Figure 2.19 and Table 2.9. The results clearly show that the active spar exhibits a higher damping and a lower vibration frequency, when compared to the active spar.

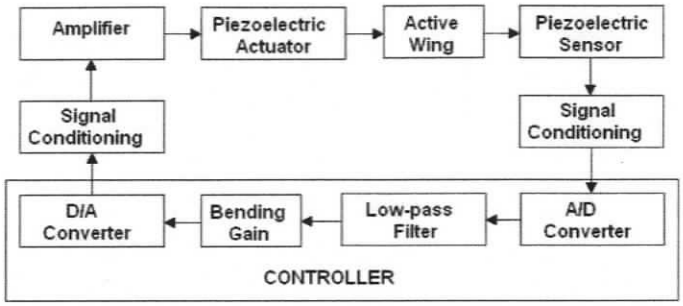

Figure 2.18 Proportional feedback control law

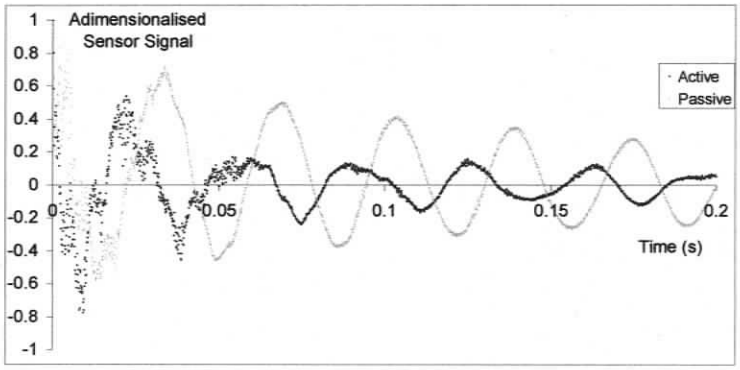

Figure 2.19 Passive and Active Responses

Table 2.9 Passive and active damping coefficients and the first natural frequency

	Damping Coefficient	f_1 **(Hz)**
Passive Spar	0.05	28.9
Active Spar	0.1	32.5
Increase	80 %	12.2 %

CHAPTER 3

WIND TUNNEL TESTS

Recalling Chapter 2, the ground vibration tests revealed an increase of 80% on the damping coefficient when using an active system. Also, an increase of 12% on the torsion-bending natural frequency was attained. This chapter describes the wind-tunnel tests and the performance of the spar in the presence of aerodynamic forces. It is expected that better results will be achieved since the aeroelastic component will enhance spar deformations due to aerodynamic forces, taking advantage of the natural torsion/bending coupling of this type of spars.

Here, the dynamic wind tunnel tests are performed on the active wing with the proposed spar design. Using the spars designed and tested in Chapter 2, a couple of wings were manufactured and tested in a wind tunnel. A brief description of the wing manufacture and mainly the tests (dynamic and especially wind tunnel tests) performed on these wings and their results are discussed. During all tasks, a comparison with the concept of a spar with zero alignment fibres is carried out to quantify the improvement in performance.

3.1 Test Considerations

The wing was designed taking in consideration the already existent RPV test platform. It was designed to fulfill the performance requirements of the RPV, namely to sustain $2.5g$ load factor manoeuvres with a structural safety factor of 1.5, taking into consideration the maximum small RPV weight of $10kg$. Other relevant physical constraints, namely wing/fuselage connection and wingspan were considered. The wing was also designed to fit in the wind tunnel test section, thus its maximum half span is 1 m.

Considering the RPV's flight envelope, required maximum wing load and already specified aerodynamic shape and airfoil (chord of 0.33 m), a wing structural model was

created in ANSYS. The airfoil used is an FX 63-137, exhibiting high lift at low Reynolds number with mild stall characteristics.

The purpose of this model is to test the multi-cell cross section spar behaviour when fitted on a real multi-cell wing. Each wing cell is a slice of the wing spar limited by two structural ribs, including the connection to the fuselage.

From flexure, torsion, buckling and vibration tests in ANSYS, critical stresses in the wing spar were identified. These are the ones that present the highest stresses and strains. Naturally, the simulation indicates that the upper and lower surfaces of the wing spar near the wing root (flexure and torsion strains) and near the wing tip (torsion strains) are the critical regions.

It is noteworthy to point out that this wing is intended to be used in the future as a specimen capable of allowing the implementation of structural health monitoring methods. This has implications in the desired PZT actuators and sensors displacement across the spar. Thus, the model was designed taking into considering two SHM methods, namely vibration and wave propagation based techniques. One main feature of the wave propagation method is that an attached wing spar rib or any kind of stiffener limits wave propagation. Thus, in order to have space to place the actuators/sensors and to allow the wave to propagate, the general structure of this small wing model for wind tunnel testing was divided only into two cells with a continuous wing spar.

However to assure the aerodynamic shape of the wing non structural ribs (not attached to the main spar) were positioned spanwise, 8 *cm* apart from each other. Beyond those two cells, there is a structural rib at the wing root and another one 4 *cm* outboard, connected to each other by foam (in addition to the wing spar).

This was intended to form a reinforced section to guarantee the wing/fuselage connection. Also, the wing skin is not structural and can be made of a transparent film, which allows viewing of the internal wing structure, actuators/sensors positioning and related systems

With respect to vibration reduction, sensors and actuators location were determined using FEM analysis of the vibration modes. This methodology revealed the location of points with larger strain values (near the wing root). The advantage provided by this approach is that a small and light actuator manages to dramatically change the vibration parameters of the wing. Also, the higher strains permit better sensing definition by the sensors, due to the larger amplitudes.

However, with respect to wave propagation methods, it is useful to position the sensors as far away as possible from the actuators. Consequently, the cells have the actuators on their root and sensors on the tip, in the spanwise direction. The disadvantage for the vibration reduction is related to the sensors amplitude output decrease and to noise percentage increase. Still, using adequate filtering and amplification, good results can be achieved.

3.2 Manufacture and Test Assembly

After the static and dynamic tests were performed on the spars to determine the mechanical performance, they were used to build the wings for wind tunnel testing. Using the same spars represents a great advantage in the precision for the wind tunnel tests, since these spars have been mechanically characterized during the Ground Vibration Tests (GVT) results.

Wings were manufactured to sustain the predicted loads. A box rib (two ribs connected to each other by foam and wood forming a box) was connected to the spar root, to allow the connection of the wing to the fuselage, and two more structural ribs, i.e., connected to the spar, one at the tip and the other at half span. A small plate (spar) is used to connect the leading edge of the structural ribs and a wood box is used to connect the trailing edge of the ribs (as trailing edge spar). However, since these structural ribs were not enough to guarantee the aerodynamic shape along the spanwise direction, non-structural ribs were used, distributed in the spanwise direction. These are non-structural ribs since they are not connected to the main spar, but just to the leading and trailing edge spars. This

configuration allows for enough free space between structural ribs to apply, in the future, health monitoring methods (both wave propagation and frequency methods). Free space means free spar surface (especially upper and lower surfaces), without any ribs attached to it, for the positioning of actuators and sensors. For example, when considering wave propagation methods, a structural rib (connected to the wing spar exterior surfaces) will act as a stringer, highly damping the propagated wave, if not totally absorbing the wave by acting as a boundary. The positions of the actuators and sensors were maintained and the same PZT actuators and sensors models were used.

The active system, meaning the electronic system, namely the signal conditioning, the control module and the amplifier, described previously were used. This system is responsible for reading the sensors and the treatment of that data, then closing the loop to apply a control law to those signals, to perform the actuation of the spar/wing. The electronic system is then responsible for the generation and conditioning of the input signals to actuators, allowing the application of the three methods of interest – vibration reduction, frequency based and wave propagation based health monitoring, by using different control laws.

In the following tests, the interest is focused in vibration reduction, namely flutter delay. The electronic system applies a feedback control law to the sensors signals to generate the signals to be sent to the actuators. That actuation is intended to counter act the deformation of the spar/wing, sensed by the sensors, and thus reduces the deformation, and vibration is attenuated. To run the tests, the wing is attached to a wood disk that allows rotation, which can simulate the variation of the angle of attack. Figure 3.1 shows the internal structure of the wing with the actuators and sensors and also the wind-tunnel setup.

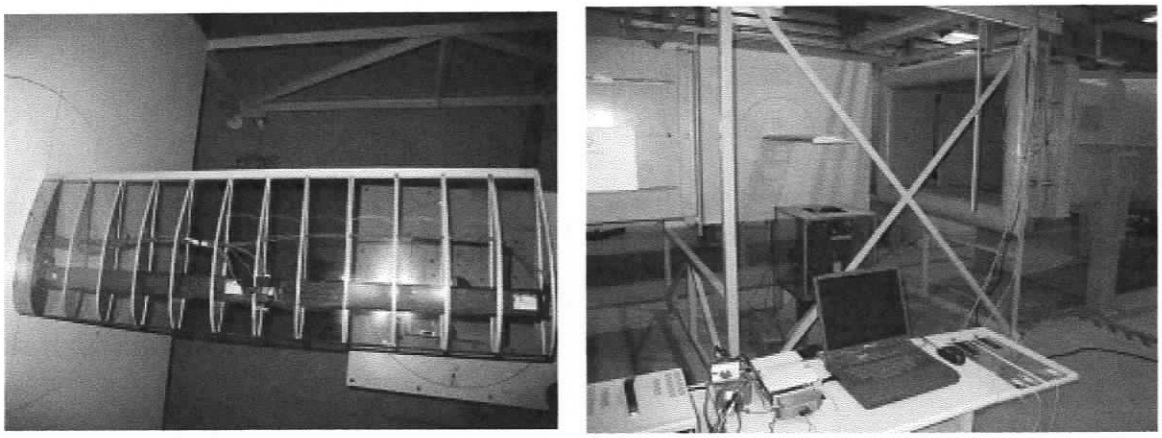

Figure 3.1 Wing internal structure and the wind tunnel test setup

3.3 Computational Models

Following the guidelines for the wing design and manufacture, a numerical model was programmed in ANSYS to assess the wing behaviour. A simple static test using the wing maximum loading was performed to check the resulting levels of stress. Afterwards, a dynamic analysis was done mainly to evaluate the behaviour when moving from a spar to a real wing. A comparison between a 0-degree fibre orientation is also presented with the objective of quantifying the resultant natural frequency differences. This way, an assessment can be done to judge if the change in the natural frequencies due to the misalignment is acceptable. Figures 3.2 and 3.3 show the finite element model, details of the spar model and the stress level contours.

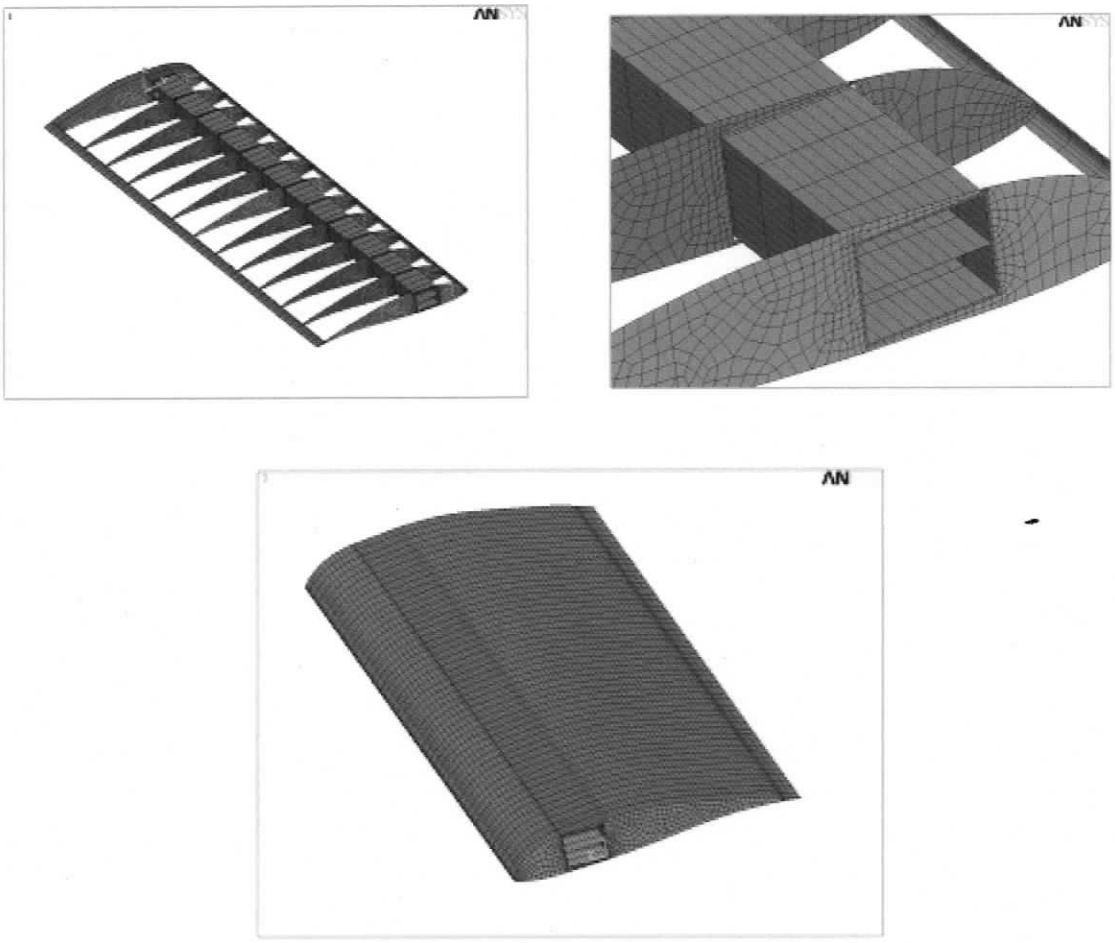

Figure 3.2 ANSYS wing model

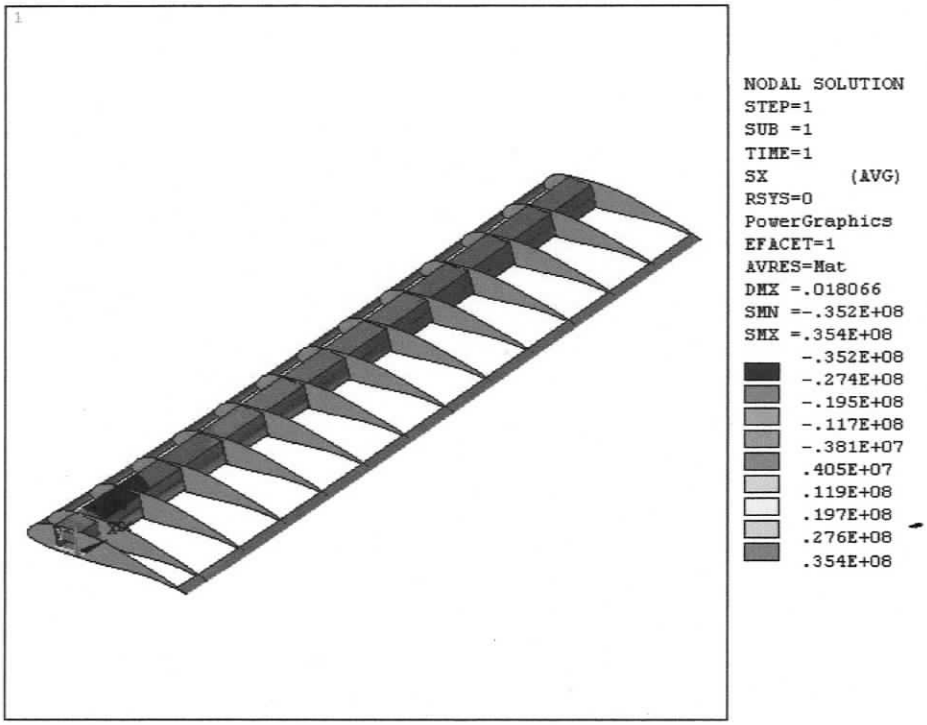

Figure 3.3 ANSYS Wing Model Stress Levels

It can be seen that the levels do not exceed the material limits thus assuring the wing safety. Table 3.1 shows the natural frequencies, attained for wings with 0 and 10 degrees fibre misalignment. Figure 3.4 shows the horizontal and vertical bending and torsion modes of vibration.

Table 3.1 0 and 10 Degrees Natural Modes Comparison

Natural Mode	0 degrees (Hz)	10 degrees (Hz)	Diff %
Vertical Bending	26.697	24.213	-9.3
Horizontal Bending	37.327	34.867	-6.6
Torsion	79.583	85.701	+7.7

1st Vertical bending mode

1st Horizontal bending mode

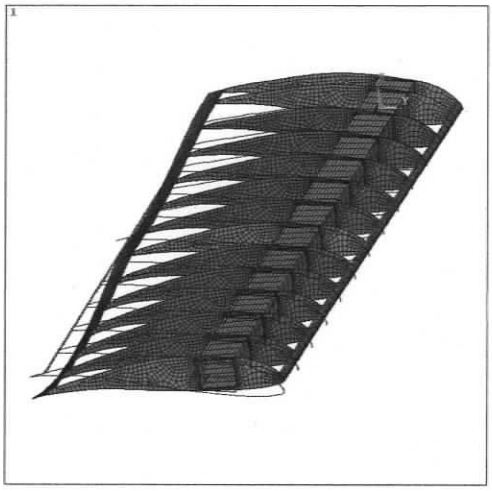

1st Torsion mode

Figure 3.4 ANSYS wing model 1st bending and torsion modes

All natural frequencies decreased, when compared to the ones attained for the spar. An increase of mass, not accompanied by an equivalent increase in stiffness, explains this observation. With respect to the torsional natural frequency this difference is quite high. This is explained by the extra mass distribution (ribs, leading and trailing edges) around the torsion axis.

Summarizing the results, it can be seen that the bending frequencies decrease, due to the loss of rigidity when there is misalignment while it increases the torsion rigidity, which results in a desired and expected increase of the respective natural frequency.

3.4 Ground Vibration Tests

GVT were performed on the complete wing to determine its first natural frequency. As stated before, a change in the value of the first natural frequency was expected, since with relation to the spar there is an increase in mass and a slight increase of rigidity. It was expected that the value of the first natural frequency would decrease, mainly due to the increase in mass.

A lateral wood wall was positioned in the wind tunnel test section, mounted on a fixed structure, independent to the wind tunnel, to reduce as much as possible the propagation of wind tunnel vibration to the wing. The wing was installed in the wind tunnel test section, clamped to the vertical wall. Then, without any flow, a shaker was applied to the wing and with the help of OROS system and using the PZT sensors signals, the wing natural frequencies were measured. A program in MATLAB was written to apply an FFT analysis to sensors signals and the results are shown in Figure 3.5

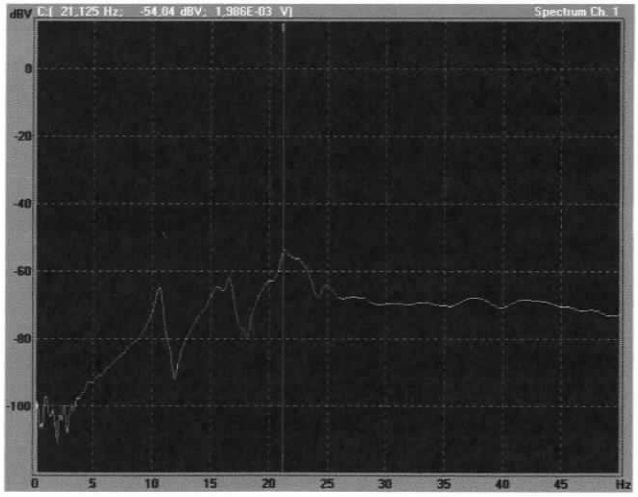

Figure 3.5 OROS 10-degree wing spectral frequencies

A value of 21.125 *Hz* was obtained for the first natural frequency of the wing, and it was observed that the wing exhibited its first natural mode (corresponding to the bending mode) of vibration when the shaker was exciting the wing at a frequency of around 21 *Hz.* This corresponds to 12.7% decrease, when compared to the FEM results

3.5 Wind Tunnel Tests

Wind tunnel tests were performed at several stabilized velocities, starting from 20m/s to 50m/s. Several feedback gains were tested and results are presented for feedback gains from 0% to 100% of maximum gain.

3.5.1 Passive and active wing tests

For each test, a sensor signal amplitude output vs. time sample was retrieved and an FFT analysis was done. For instance, Figure 3.6 represents the FFT results obtained for the 20 *m/s* velocity for the passive wing and active wing with a gain of 50% max.

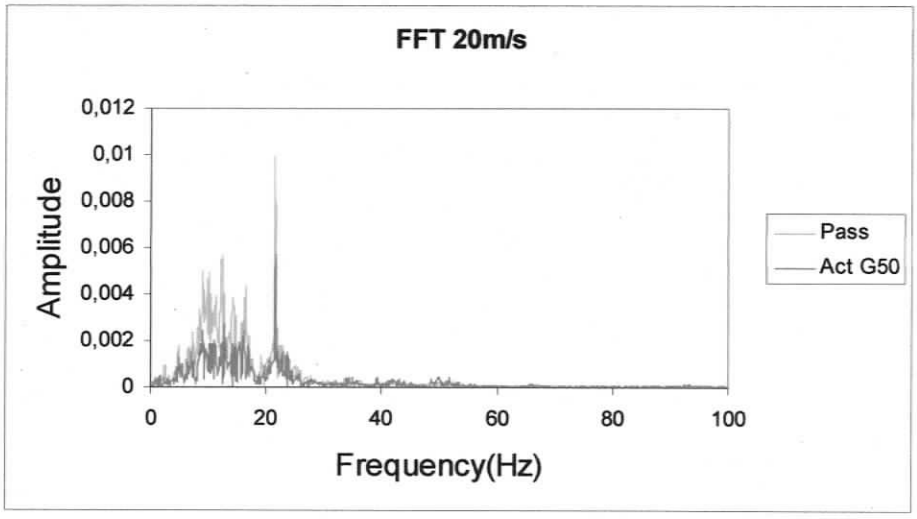

Figure 3.6 20m/s passive and active wing FFT analysis

Observing the different FFT analysis conducted for each test, it can be seen that the 1st wing natural frequency, which corresponds to a bending mode, appears around 21 *Hz.*

This conclusion was reached since it is the most significant peak and the one that is most correlated with velocity.

The peaks around 10 *Hz* corresponds to the wind tunnel natural frequency and airflow pulsation (as proved by the tests preformed to measure wind tunnel and its structures natural frequencies – without the wing installed). These peaks grow higher and strongly influence output data for velocities between 25 *m/s* and 35 *m/s*. Adding to this, for velocities above 45 *m/s* the wing's vibration level is very high. From the experiments run at both velocity intervals, it was concluded that the data retrieved was not valid. In conclusion, tests were run for speeds between 20 and 25 *m/s*, and between 30 and 45 *m/s*.

The results for 20, 30, 40 and 45m/s with gains of 25, 50, 100% are plotted in Figure 3.7. After post processing it was found that these parameter sets were representative of the general behaviour. Maximum signal output amplitudes were recorded and the amplitude decreases from passive to active tests. Generally, this amplitude tends to be smaller when a higher gain is applied.

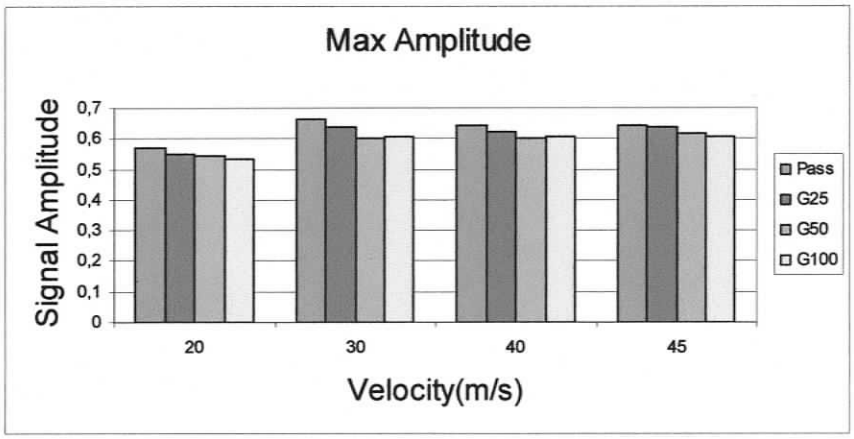

Figure 3.7 Wing maximum amplitude

Figure 3.8 shows the percentage of maximum sensor signal output amplitude decrease – a maximum 8.8% decrease is reached for 30 *m/s* of velocity and a gain of 50% max.

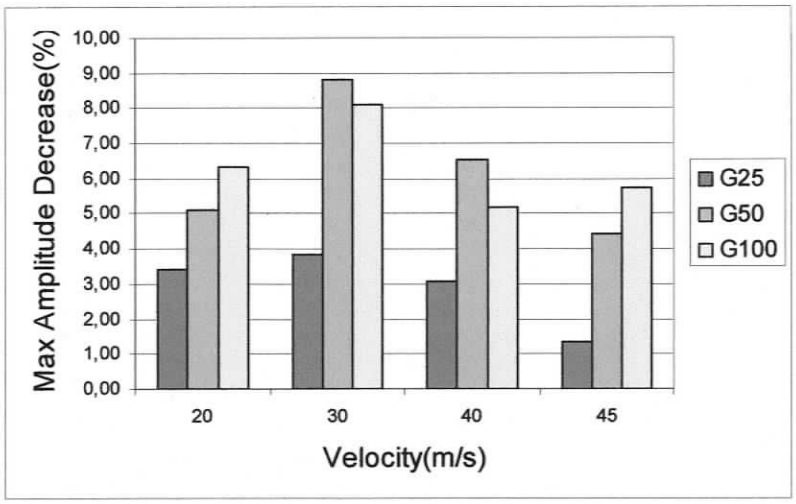

Figure 3.8 Wing maximum amplitude decrease

Concerning the damping analysis, studies were concentrated around the 1st natural frequency. Having the sensor signal output FFT amplitude vs frequency graphs, damping is calculated by retrieving the frequency value for the peak amplitude and frequency values (around the previous) obtained for maximum amplitude divided by the square root of 2. With these 3 values it is possible to determine a damping coefficient proportional value (not the damping coefficient itself), by subtracting the highest and lowest frequency values divided by the central frequency one [45].

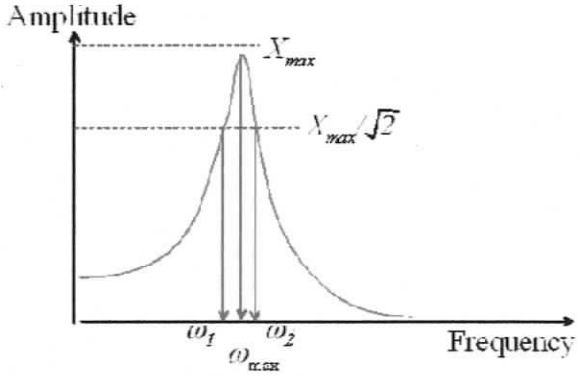

Figure 3.9 Typical frequency spectrum [45]

As explained, the damping coefficient, ζ, can be determined by the equation (3.1),

$$\zeta = \frac{\omega_2 - \omega_1}{2\omega_{max}} \tag{3.1}$$

With this algorithm all the damping coefficients were calculated and plotted on the same graph along with the respective quadratic polynomial trend lines as shown in Figure 3.10. These lines allow prediction of the flutter speed (corresponding to the velocity for zero damping coefficient, i.e. when the trend lines would ideally cross the velocity axis).

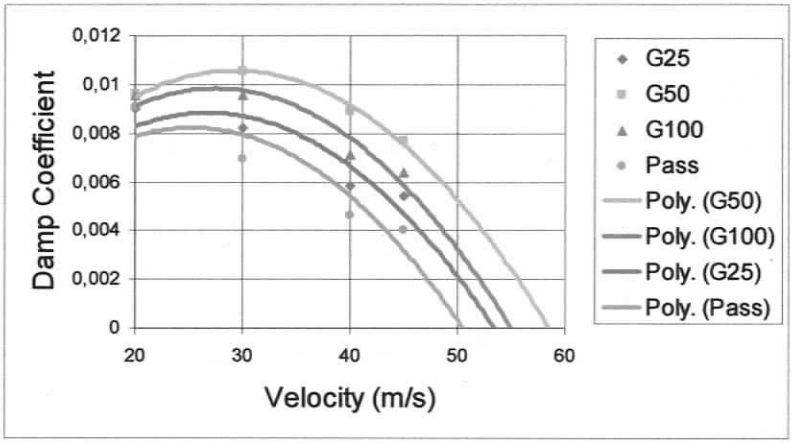

Figure 3.10 Damping for 25, 50 and 100% of maximum gain

Inspecting the plots, the flutter speed increases from passive to active tests, and it reaches its highest value for the 50% maximum gain. Also, damping improvements are observed from passive to active tests, and they are higher also for the 50% maximum gain. Over actuation and delays influence the active gain results for gains higher than 50%, resulting in poorer outcomes.

Figure 3.11 shows the percentage damping improvements - a maximum of 92.6% improvement is reached for 45 *m/s* of velocity and a gain of 50% max.

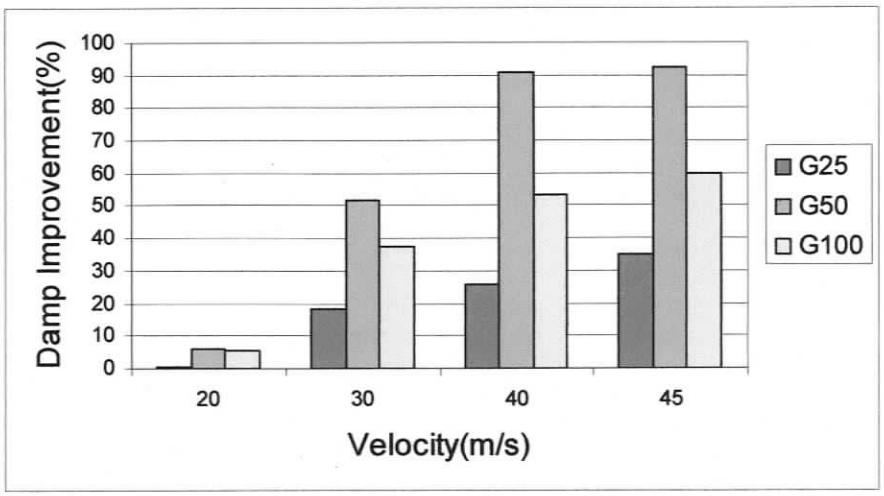

Figure 3.11 Damping improvement for 25, 50 and 100% of maximum gain

The maximum damping improvement, obtained in the wind tunnel tests, is higher than the one obtained for the spar when its mechanical tests were performed (80% max improvement). This increase can be explained by the BTC, which had no influence on the spar behaviour when the mechanical tests were done, but which is essential on wind tunnel tests as this coupling affects the aeroelastic behaviour of the wing. When the wing bends and consequently rotates along spanwise axis due to the coupling, the aerodynamic of the wing is influenced, i.e., aerodynamic loads applied and their distribution is altered, affecting the wing structure, changing consequently the wing structure deformations.

3.5.2 Baseline zero-degree passive wing comparison

A similar spar was manufactured but with no misalignment and incorporated into a wing. Only one sensor was installed because the only aim it to test the passive behaviour for comparison purposes. With the wing mounted on the wind tunnel, OROS was used to determine the wing first natural frequency. A value of 24.374 *Hz* was obtained, which is very similar to the computational one but with a decrease of 12.4%. Wind tunnel tests were performed for the same stabilized velocities as before. The results attained are presented in Figures 3.12 and 3.13.

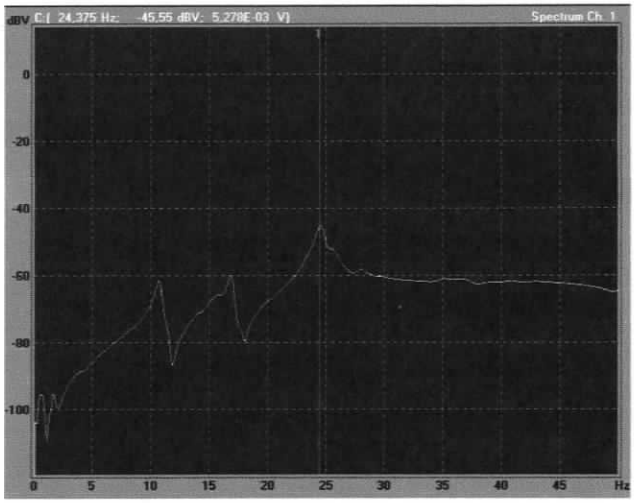

Figure 3.12 OROS 0 Degree Wing Spectral Frequencies

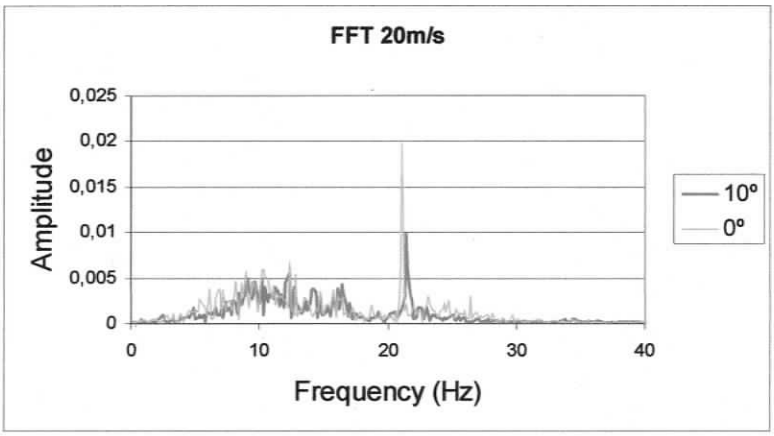

Figure 3.13 0 and 10 Degree Passive Wing FFT Analysis

The figures show two main aspects. The first is the expected amplitude decrease when there is misalignment. The 10-degree spar reacts with torsion when bent. In this case, the vibration amplitude is decreased. The second one is the unexpected natural frequency similarity. The structural excitation is now done by the airflow. In this case, for the same speed, the airflow frequency must be around 20 *Hz*. In this region, both wings start showing the first natural mode, thus explaining the reason the same frequency appears for the two different wings.

Concerning the first natural frequency decrease, it should be expected when there is misalignment, because for the same mass, the rigidity gets lower for the vertical bending motion. This was also shown by the computational results. It can be seen also, that the experimental results are lower than the computational ones, in both cases. The reduction and its magnitude can be related to manufacture issues. Both spars do not represent truly 100% the models created in ANSYS. Figure 3.14 shows the amplitude variation for both spars at different velocities.

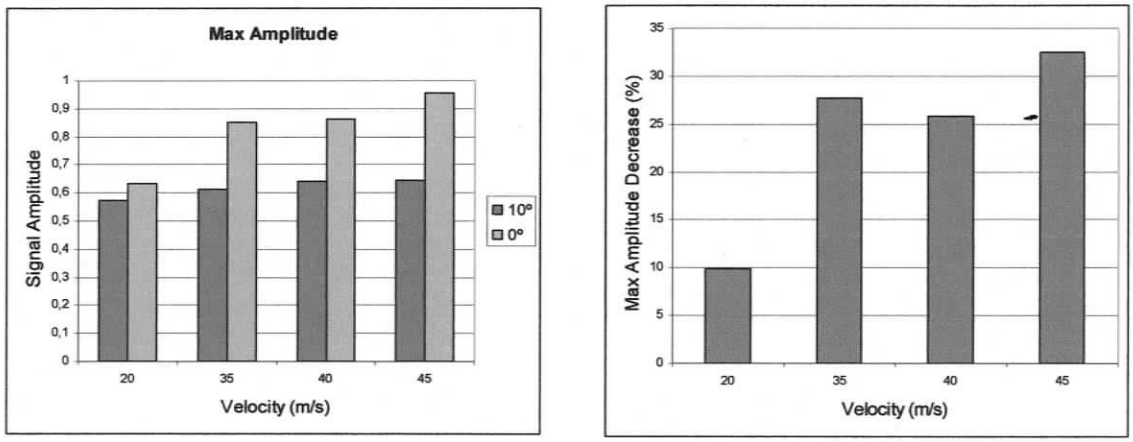

Figure 3.14 Zero and 10-degree maximum amplitude

In conclusion, one can say that the misalignment on spars (to a certain extent), by itself, can lead to an improvement in the wing's behaviour. Additionally, it can be clearly augmented by implementing active control techniques.

CHAPTER 4

FLIGHT TESTS

The performance of the wing was successfully quantified and the results in the wind-tunnel were encouraging. But the final objective of the thesis was to test the active multi-cell cross section spar wing in real flight operation conditions. A remotely piloted vehicle has been developed earlier to test other active aeroelastic control concepts. This RPV was used here to test the active wing. In order to do so several aspects must be taken into consideration. The first aspect is related to the required wing modification. The flight test control model was updated in order to be suitable for flight testing data acquisition. Furthermore, the data acquisition and control equipment must be installed in the aircraft under space constraints. For the ground vibration and wind tunnel tests, external power and amplifiers were used. For flight test conditions, a battery must be used to supply power and an internal amplifier must be used.

In this chapter, a flight performance assessment is carried out and the lessons learned in the wind tunnel tests are applied here such as the determination of important system parameters. The engine influence on the sensor systems is also studied. The flight test was carried out at the Air Force Base in Sintra, Portugal.

4.1 Wing Modifications

In order to install the wing on the RPV, some modifications had to be done. These modifications did not compromise the integrity of the tests but the overall changes resulted in a slight mass increase of the wing. The wing, shown in Figure 4.1, was equipped with an aileron and respective servo action mechanism. Its root was reinforced in order to receive the clamping pin for attachment to the fuselage.

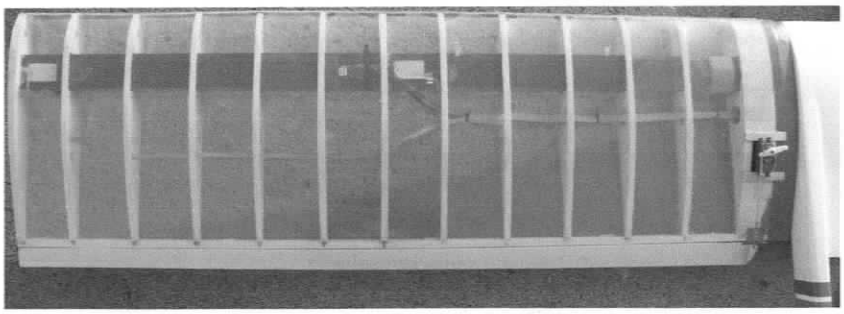

Figure 4.1 Flight test modified wing

4.2 Flight Test Control Model

The previous control system architecture used in wind tunnel tests was used with slight modifications. The DSPACE module is capable of operating as a stand alone system, i.e., without being connected to a laptop. Thus, the control model has to be uploaded to its memory. It is also able of storing 16Mb of flight data. This data can be downloaded to a laptop after each flight. It is important to be very selective on the data to be saved during flight because the flash memory available onboard is very limited.

Another important aspect concerns the desired data analysis for future post processing. Since the aim is to test the wing behaviour difference between passive and active solutions, both must be tested under similar circumstances. To do so, the control system must be enabled and disabled automatically. All these requirements resulted in the control model illustrated in Figure 4.2.

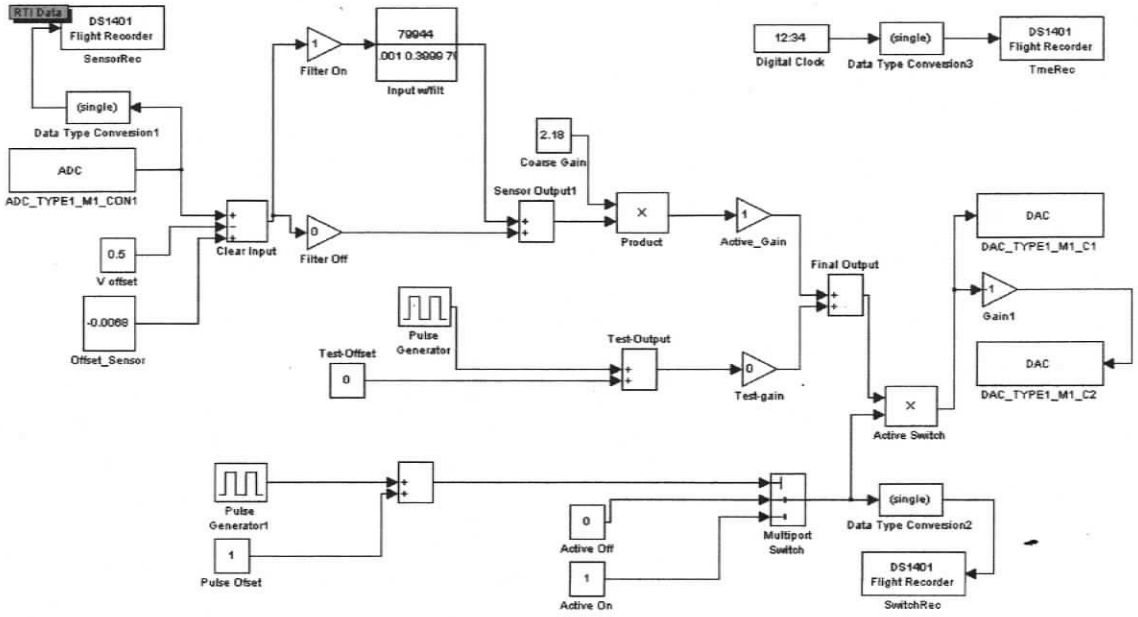

Figure 4.2 Modified flight test SIMULINK control law module

As it can be seen, this control model is very similar to the one used by the active wing in the wind tunnel tests. However, in the first instance they must be converted to single data type in the Data Converter block and then sent to DSPACE Flight Recorder block. The recorded variables chosen were the pre-filtered sensor output, switch record and time. The sensor output is crucial for the analysis to be performed.

A digital clock block provides the simulation time, starting when DS1401 runs the control model file loaded in the flash memory. Its important since it gives information related to the beginning of the flight testing. The switch command signal is a pulse signal (0 or 1) added to 1, resulting on a square wave with values 1 or 2. If this wave takes the 1 value, the active system is turned off, and if it takes the 2 value, it switches it to on. The period of the pulse wave is 24 s. With this system there are 12 s with controller OFF and 12 s with controller ON. With this information the output data can be split and compared. Finally, the data acquisition rate was set to 1KHz. This way approximately 9 minutes of flight testing data can be stored, which is suitable for present needs.

4.3 Ground Vibration Testing

A series of ground tests were conducted to evaluate and verify the active system behaviour on the RPV platform. It includes amplifier and power supply testing. It also included the engine influence on the sensors reading. As it was previously referred, an external amplifier was used to carry out all the tests done on both spar and wind tunnel test chapters. Since this amplifier cannot be transported on the RPV due to its dimensions and power needs, another amplifier has to be used. This requires new tests to set the proper gain to be used. To do this, the RPV was put in the wind tunnel as illustrated in Figure 4.3. This allows the creation of a random pattern of inputs to the system and evaluating its response.

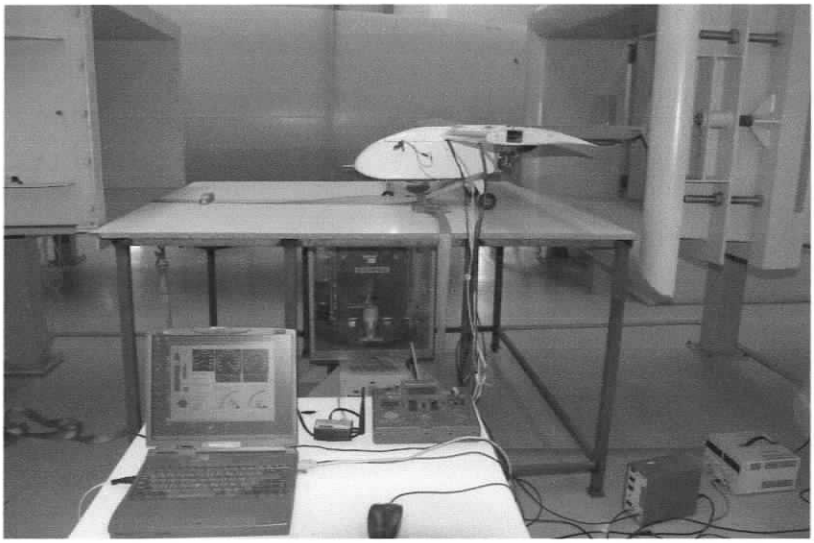

Figure 4.3 RPV wind tunnel test setup

After running similar tests to the ones done on the wind tunnel, it was found that a gain of 21.8 % produced the best active response possible. The next task was to compare the different amplifiers response. For identical wind tunnel flow conditions the responses illustrated in Figure 4.4 were recorded. Consider that when the black horizontal line is 1 the active system is ON, when it is 0 the active system is OFF.

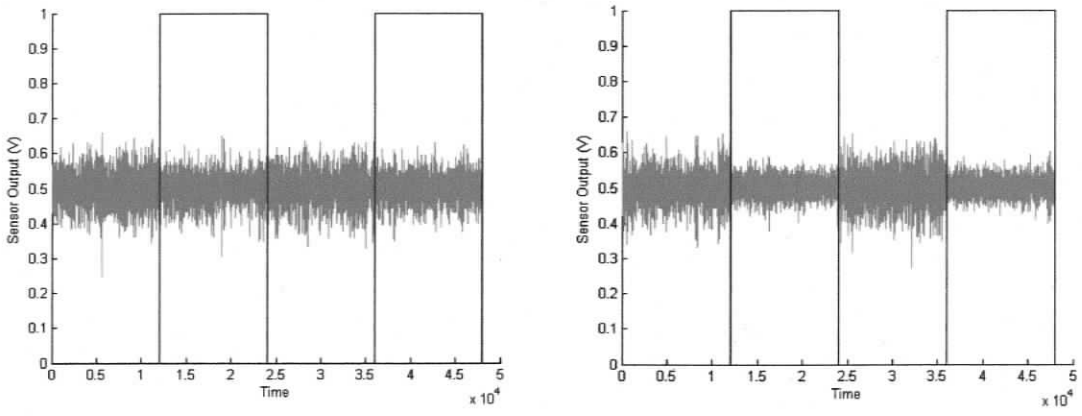

(A) (B)

Figure 4.4 Active mode with internal (A) and external (B) amplification

The vibration reduces when the active system (when the black horizontal line has a value of 1), on both figure 4.4 (A) and (B). But a significant actuation decrease is observed in (A) which compromises the level of vibration attenuation expected. This is a natural consequence due to the use of a less responsive amplifier. Both voltage and current output limits are significantly lower for the internal amplifier. For instance, the maximum output voltage decreases from 200V to 140V, which represents -30% of actuation capability. Nonetheless, there is a vibration amplitude decrease. The FFT analysis shown in Figure 4.5 leads to the same conclusion.

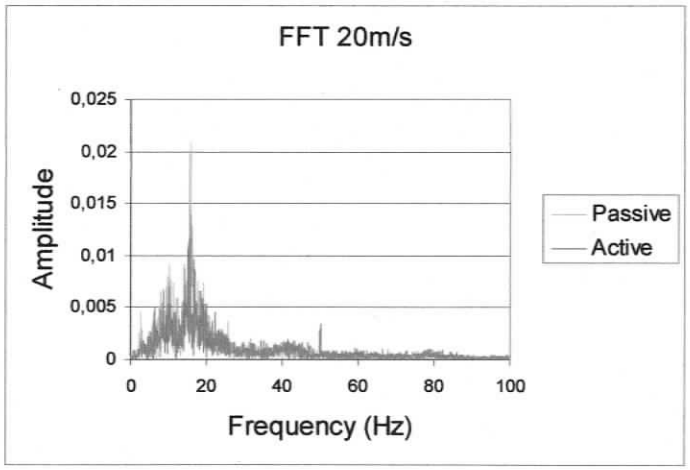

Figure 4.5 Internal amplifier response FFT

An interesting fact is the observed 1st natural frequency decrease. When the wing is mounted on the RPV, the rigidity offered by its root is less than the one obtained in the wind tunnel wall. Adding to this, the aileron installation with the respective servo contributes to a mass increase. The difference between powering the system with external power supplies and batteries was also studied and no significant was seen.

After setting up the RPV with all the necessary equipment, pre-flight tests were done to check for interferences between the equipment. The engine was started in and the flight surfaces control was tested. No electrical interference was observed. Afterwards, the data was collected from the DSPACE recorder to check the sensors reading. Figure 4.6 shows the sensors reading starting from the engine on idle (until 7000ms) and afterwards at its maximum power. It shows that when the engine is running, it severely affects the PZT sensor readings. Due to this, it was decided to perform the tests on gliding flights. This way, the active system and necessary operating gear can be tested without the engine's influence.

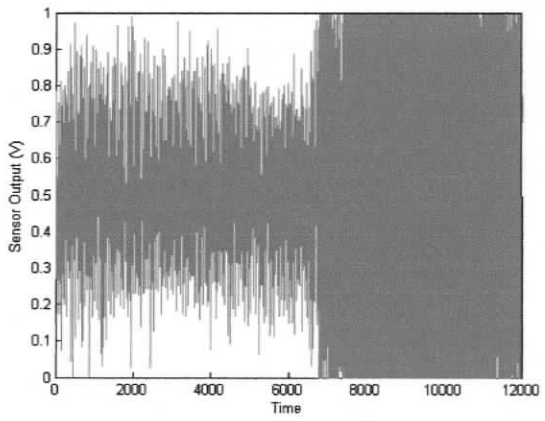

Figure 4.6 Engine and sensor reading interference

The interference origin between the PZT sensors signal and the engine was not determined. Possibly is related either to electrical interferences, related to the sparks released on the engine's cylinder or to spar's resonance excited by the engine vibrations.

4.4 Flight Test Descriptions

For this test, besides the normal flight equipment of the airplane, the RPV was equipped with:

- DSPACE to act as the control unit and data recorder;
- Signal conditioning module board;
- One SA-10 power amplifier for the actuators;
- One pitot system with telemetry so that the speed of the RPV could be monitored on the ground in real time;
- Several packs of batteries to power both the flight controls and all the equipment stated.

The equipment set up onboard, shown in Figure 4.7, took into account the RPV's mass balancing.

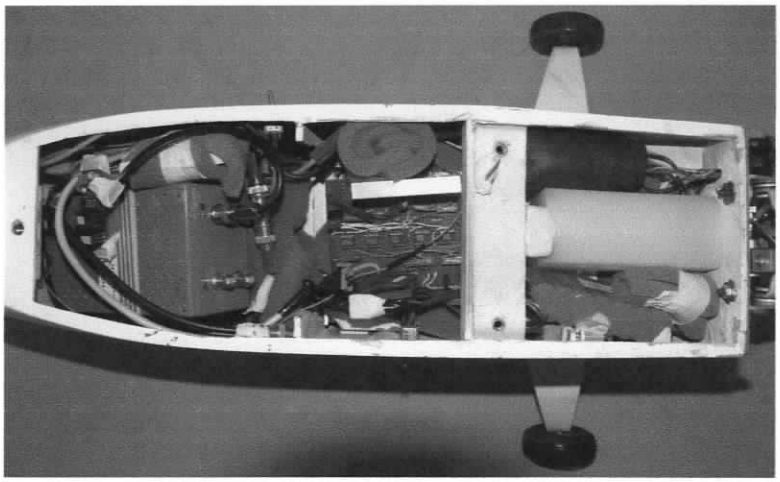

Figure 4.7 RPV internal equipment placing

The procedure consisted of flying the RPV as high as possible, which was limited by the pilot's observation capability. Afterwards the engine was cut off and a glide descent targeted at a speed of 20m/s was done. The airspeed was monitored using the laptop with the Jet-Tronic software, which received the pitot telemetry signal from onboard, and the

testing time was being correlated with speed and both values registered. This operation turned out to be very difficult to do, even with two assistants, because of the difficulty in keeping constant conditions. The RPV is shown in Figure 4.8 on the runway before the flight tests.

Figure 4.8 Flight test setup on runway

4.5 Flight Test Results

Two consecutive flights were carried out. Figure 4.9 shows the flight data recorded, which includes the PZT sensor signal, the ON/OFF active system indication and the flight time (ramp lines). Each ramp represents one flight, so two flights are shown. Since the active gear power was disconnected between the two flights, the time line becomes zero on the beginning of the second flight. Note that, time is always measured in ms and the output voltage from the PZT sensors is proportional to the wing vertical vibration (p.36). Consider that when the black horizontal line is 1 the active system is ON, when it is 0 the active system is OFF (p.58).

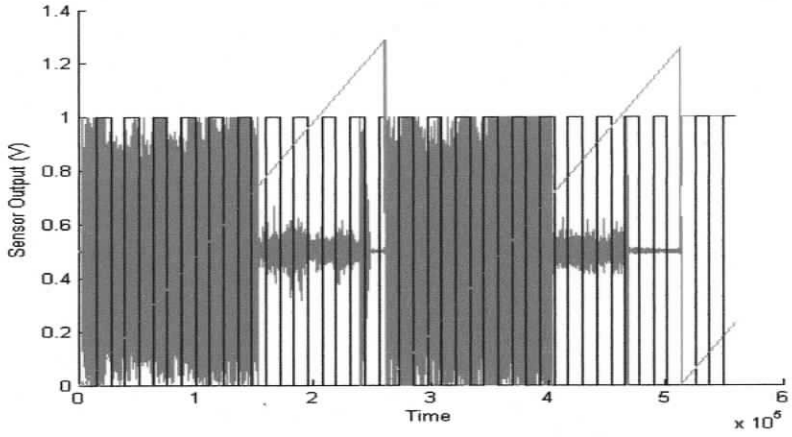

Figure 4.9 Flight test sensor readings

On the first flight the engine was shut down at approximately $1.5x10^5$ ms. The second flight starts with the second ramp and the engine was shut down at approximately $4.05x10^5$ ms.

Figure 4.10 show the PZT sensor readings for the glide part for both test flights.

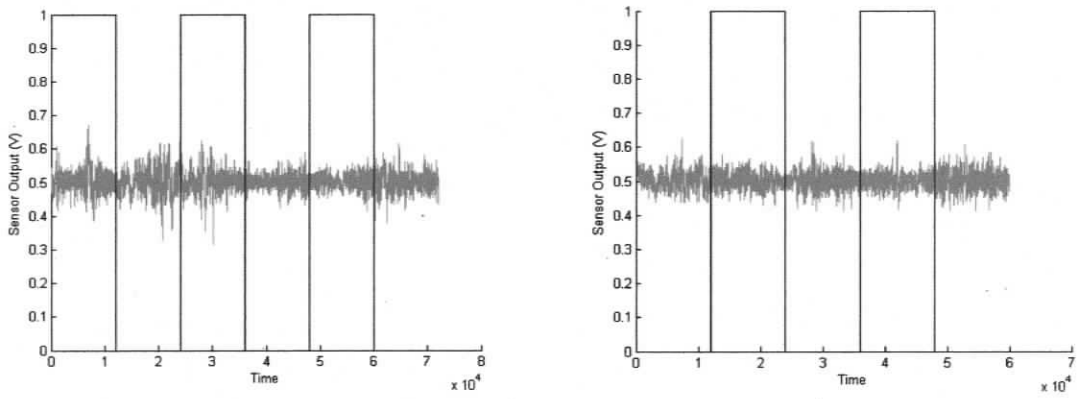

Figure 4.10 1st (A) and 2nd (B) gliding flights sensor output

The aircraft was flown within sight of the pilot, and it performed a series of turns that influenced the results. In the turns, effective wing lift increased and the vibrations were

higher. This may explain why sometimes when the control was ON (and was supposed to decrease vibrations) some very large amplitude peaks appeared. Due to this, no maximum or minimum comparison is done because they do not represent a typical behaviour.

If one considers that a window represents a state of active or inactive, flight 1 has 6 windows and flight 2 has 5 windows. Figures 4.11 and 4.12 show adjoining data acquisition windows and these are indicative flight conditions obtained using FFT analysis.

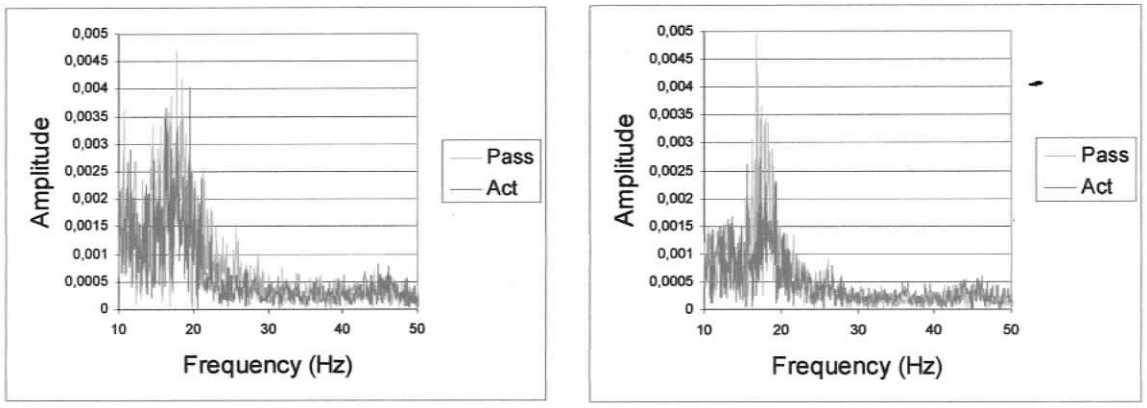

(A) (B)

Figure 4.11 $2^{nd}/3^{rd}$ (A) and $5^{th}/6^{th}$ (B) data windows for passive/active FFT analysis

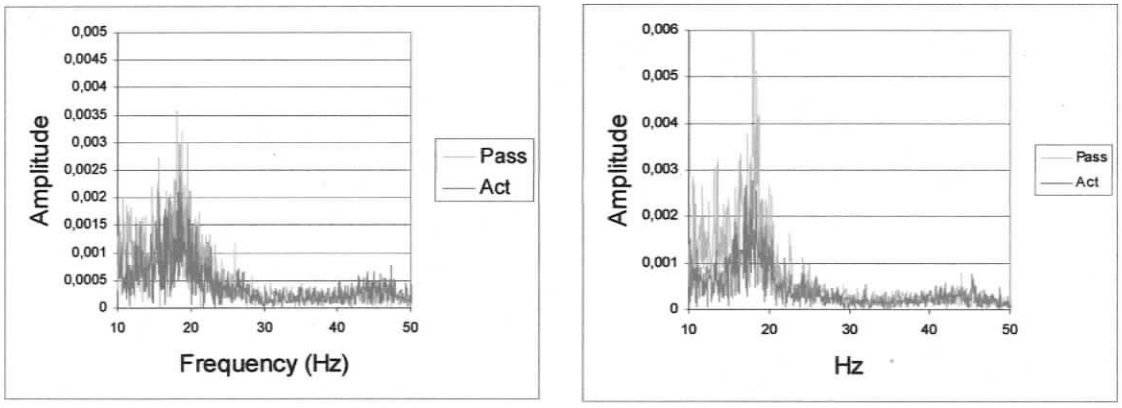

(A) (B)

Figure 4.12 $2^{nd}/3^{rd}$ (A) and $4^{th}/5^{th}$ (B) windows for passive/active FFT analysis

A clear improvement can be observed. Another interesting fact is that the improvement seems to be higher in the last part of both flights, the final straight line approach. This can be explained by the fact that the wind conditions were more severe near the ground thus implying more vibrations on the wing. Furthermore, since the airplane was aligned with the runway, less pilot's inputs were necessary to guide the RPV to the landing.

Summarizing, the flight tests were successful and very valuable lessons were learnt on the behaviour of the active spar wing under real operational conditions.

CHAPTER 5

CONCLUSIONS AND FUTURE WORK

The proposed solutions have resulted in a successful implementation of a new spar concept on a conventional wing. The proposed solutions consists of a multi-cell cross section spar with misaligned fibres, which resulted in an improved aeroelastic performance and suppression of vibrations and consequent postponement of flutter.

The first step in the process was to design of the spar itself. The conceptual design of the spar indicated that it should have more than one section, and the fibre orientation should be aligned at an angle with respect to the spanwise direction. On a plan view, these fibres must start in the trailing edge and end in the leading edge such that the leading edge decreases its displacement when the wing experiences a lift load. For a simple constant rectangular cross section spar with an overall constant thickness and manufactured with one material, this is the only way of achieving the desired bending torsion coupling (BTC).

Next, the issue was to decide the final dimensions and the right misalignment of the fibres. On one hand, a small misalignment could result in a poor BTC but good vertical stiffness and high natural bending modes frequencies. On the other hand, a high misalignment would present a better coupling but poor stiffness and low natural bending frequencies. To determine the best solution, an optimization problem was defined and solved. The constraints were defined. The design variables were found to be the width, misalignment and wall thickness. For the definition of the objective function, the parameters found to be critical were considered: the mass, for its importance in airframe design, and the first natural frequency, for its influence in the flutter behaviour and the coupling. With the set of design variables, constraints and objective function, an optimization problem was formulated and solved. Two methodologies were used. The first one was based on the commercial software ANSYS. The other one was programmed,

based on metamodeling. Since ANSYS was used to calculate the objective functions value, it works like a black box and it cannot be represented by an analytical function. The second method was developed using a global optimization problem approach to validate the ANSYS solution. The final solution uses the minimum geometric constraint values, which is natural to achieve the minimum weight objective. The fibre misalignment is a compromise between the vertical stiffness and coupling. The final result presented approximately 6.22 degrees misalignment.

At this point, manufacture issues were considered. The possible imprecision in the layer placement presented a problem. A sensitivity analysis was run and it was decided to place the fibres with a 10 degrees orientation. The safety margins and precision were higher with this value.

Having obtained the optimal design, computational models obtained in ANSYS were compared with experimental ones. An important conclusion arose from this task. The selected manufacturing process was not the most adequate to provide the compression levels necessary to attain the ideal carbon composite characteristics. At this point, a correction to the Young's Modulus was done, based on experiments and computational models. As expected, the desired behaviour was obtained and the main objective was not affected.

The use of active materials was tested right way at this very early stage of work. PZT sensor and actuator positions were carefully studied. Having in mind future objectives, such as structural health monitoring, besides vibration reduction and flutter suppression, two pairs of actuators were used, one at the root and the other at the midspan. In each case, one actuator was glued on the upper and the other on the lower part of the spar. Two pairs of sensors were also glued to the spar, but for this work, only one was necessary. Its position is at the midspan and both upper and lower positions were suitable for its task.

Experimental active tests were then run and compared to passive ones. The active methodology consists of reading the sensors strain and feeding the signal back to the

actuators, via a proportional control system, to oppose the movement. Substantial damping and torsional natural frequency increases were attained. This presented a good motivation for continuing the path followed so far.

At this stage, the next milestone was identified. A wing was to be built with one of the spars manufactured. Since this spar is intended to be used for future SHM methods testing, a wing composed of two main cells was designed. One of these methods is based on wave propagation. Starting from the root, this wing has a reinforcement box for clamping both on the wind tunnel and RPV fuselage. Then it has two spanwise cells. Each one is defined by two structural ribs (attached to the spar). Between these two, there are "form" ribs, which are not attached and are placed to guarantee the airfoil shape and transmit the aerodynamic loads to the edges. These are then transmitted to the spar by the attached structural ribs. This way, mechanical waves generated by the actuators can progress through the spar in each cell.

Next, wind tunnel tests were carried out. These were run at several stabilized velocities, starting from 20m/s to a maximum near the flutter speed initiation behaviour, approximately around 50m/s. A similar wing was built at the same time, using a 0 degrees spar with the same weight. This allowed comparing the benefits resulting from the misalignment only, no active systems were considered at this stage. The results showed that the native behaviour is clearly improved when applying a misalignment to the fibres (which produces the BTC desired effect). An approximately 30% reduction in the maximum vertical displacement amplitude was found for a test run at 45m/s. It also presented a stable vertical displacement behaviour as the velocity was increased. The 0-degree spar tended to increase this parameter as the velocity was risen.

When applying active control using the PZT actuators, this aeroelastic performance of the wing was enhanced. A structural damping increase around 90% was attained for 45m/s. The flutter was predicted to be delayed by 8m/s, which corresponds to a 16% increase.

The best results where found when using a 50% gain increase in the proportional feedback control system.

At this stage, the second milestone was completed and the main objective of the work satisfied, since the wind tunnel tests closely reproduce the structure's response to the real airflow inputs. Nevertheless, flight testing can push the limits and test other aspects also determinant of the systems' viability. So, the final milestone was to adapt this wing to the RPV and test it in flight. To do so, the control equipment had to be put onboard. The energy source was changed to batteries and an RPV indicated airspeed measurement equipment was installed in the RPV. The RPV was manually piloted from the ground. The control system was pre-programmed with the control law and set to save all the flight data for future post-processing. During the flight, the active system was automatically set on and off in intervals of 12s. Pre-flight tests revealed engine interferences of undetermined source. Gliding flight option were used for testing and spectral frequency analyses were carried out on the data. The results showed a significant vibration reduction, despite the reduced available amplification provided by the internal amplifier.

This final work stage closed the loop of the spar development and on the passive and active system implementation. As a final conclusion it can be said that both the passive and active multi-cell cross section spars proved to be a viable solution in active aeroelastic control solutions in flight vehicles.

As for final remarks, no reliability aspects regarding the interaction between the actuators and the structures were considered. This field is presently subject of several investigations and is not one of the present work objectives. Results from upcoming investigations will hopefully provide some enlightening over this real concern.

The BTC spars had already been theoretically explored in the past. So far no one had run wind tunnel or flight testing on this concept. Through this work, a major contribution to the future application of such spars on single spar wings is offered. RPVs and small light manned aircrafts are possible applications examples. Also, it also enhances the

application scope of active structures and reinforces the benefits stated on previous and present works on the same area.

5.1 Future Work

There is much that can be done in the future to improve this work, at almost all levels. With better tooling and manufacture capabilities, spars without the midwall and with better mechanical characteristics can be manufactured. This way, weight can be significantly decreased and the performance can be increased. More complex ideas such as shape and thickness changing spars can also show advantageous coupling behaviour. This opens other fields of study of active material implementation.

The active control system can be also improved. Proportional-Integral-Derivative (PID) laws implementation can be used to provide more accurate and complete data about the spar's displacement and behaviour. With this, better retroaction algorithms can be implemented, augmenting the general performance of active systems (the spars curvature may be important to tune up the active system and also provide important data for SHM algorithms).

The use of optical fibres as sensors, namely Fibre Bragg Grating sensors, can push forward the quality of the sensor's signal. This type of sensor is very promising, namely for SHM purposes. In the concept developed in this work, the vibration reduction aim can benefit if these sensors are installed. They can thus be used to perform both tasks at the same time.

A problem still arises regarding the equipment necessary to practically implement such a system. At the present time, the necessary equipment (ex: interrogators) dimensions and weight are inadequate for flight testing but already suitable for wind tunnel tests.

It is intended to eventually apply embedded PZT actuators. PZT layers are already commercially available with preferable orientations. As they can be laid up during the manufacturing process, an internal and increased actuation can be achieved. Also, the

research on better commercial amplifiers, suitable to be carried on board should be carried out. This is a relevant link in the active system chain, for flight testing.

Finally, it is believed to be worthwhile to study the implementation of the concepts studied during this project on a larger scale flight demonstrator. The scale factor is very important when moving towards future commercial application. On one hand, adaptive materials are in constant development and improvement. Hopefully, this will lead to better intelligent materials with a large actuation and faster response speed. On the other hand, the BTC spar can be immediately applied. With the present sensors and technology this can be done in the near future, as the Portuguese Air Force Laboratory already has a 2x scale of the RPV used in this study.

REFERENCES

[1] Bisplinghoff, R.L., Ashley, H., Halfman, R.L. "Aeroelasticity", Dover Publications Inc, New York,1996

[2] Njuguna, J., "Flutter prediction, suppression and control in aircraft composite wings as a design prerequisite: A survey", Wiley Interscience, 2006

[3] Gomes, M.A., "Modelação e Optimização de Estruturas Adaptativas Electromecânicas", MaSC Thesis, Instituto Superior Técnico, Portugal, 1997

[4] Kudva, et al., "Overview of the DARPA/AFRL/NASA Smart Wing Program", SPIE 3674-230, US, 1999

[5] Pach, L.G., Joslin, R.D., "Overview of Active Flow Control at NASA Langley Research Center", SPIE 3326-22, US, 1998

[6] AGARD Symposium on Smart Structures for Aircraft and Spacecraft, AGARD-CP-531, Lindau, Germany, 1992

[7] RTO Symposium on Structural Aspects of Flexible Aircraft Control, Ottawa, Canada, RTO-MP-36, 1999

[8] Becker, J., Luber, W.G., "Comparison of Piezoelectric Systems and Aerodynamic Systems for Aircraft Vibration Alleviation", US, SPIE 3326-04, 1998

[9] AGARD Sympoium on Future Aerospace Technology in the Service of the Alliance, AGARD-CP-600-Vol.1, Palasiseau, France, 1997

[10] Schetky, L., Steinetz, B.M., "Shape Memory Alloy Adaptive Control of Gas Turbine Engine Compressor Blade Tip Clearance", US, SPIE 3326-36, 1998

[11] Simpson, J., Schweiger, J., "Industrial Approach to Piezoelectric Damping of Large Fighter Aircraft Components", US, SPIE 3326-06, 1998

[12] Wilkie, W.K., Park, K.C., "An Aeroelastic Analysis of Helicopter Rotor Blades Incorporating Piezoelectric Fibre Composite Twist Actuation, US, NASA Technical Memorandum 110252, 1996

[13] Cesnik, C. E. S. and Shin, S. J., "On the twist performance of a multiple-cell active helicopter blade", Institute of Physics Publishing Smart Materials and Structures, 10, 53–61, 2001

[14] Schewiger, J., Sensburg, O., "A critical review of efforts and achievements to improve aircraft performance or efficiency by active structures concepts", Proceedings of the International Forum on Aeroelasticity and Structural Dynamics – IAFSD 2001, 2001

[15] Voracek, D., Pendleton, E., Griffin, K., Reichenbach, E., Welch, L., "The active aeroelastic flight research program", In Symposium on Novel and Emerging Vehicle and Vehicle Technology concepts, 2003

[16] "Active Aeroelastic Wing", (n.d.), Retrieved February 5, 2007, from http://www.nasa.gov/centers/dryden/news/ResearchUpdate/AAW/index.html

[17] Kouzmina, S.I., et al., "Some applications of active aeroelasticity concept to aircraft design". Proceedings of the International Forum for Aeroelasticity and Structural Dynamics – IFASD 2001, 2001

[18] Lazarus, K.B., Crawley, E.F., Bohiman, J.D., "Static aeroelastic control using strain actuated adaptive structures", 1st Joint US-Japan Conference on Adaptive Structures,1990

[19] Lin, C.Y., Crawley, E.F., "Towards Optimal Strain Actuated Aeroelastic Control", PhD Thesis, Massachusetts Institute of Technology, US, 1996

[20] McGowan, A.R., Heeg, J., Lake, R.C., "Results of Wind-Tunnel Testing from the Piezoelectric Aeroelastic Response Tailoring Investigation", AIAA-96-1511-CP, US, NASA Langley Research Center, Hampton Virginia, 1996

[21] Suleman, A., Costa, A.P., Moniz, P., "Experimental flutter and buffeting supression using piezoelectric actuators and sensors", Proceedings of the Smart Structures and Materials – 3674, 1999

[22] Ameduri, S., "Design and realization of a sma torque tube aimed at defecting and morphing aerodynamic surfaces", Proceedings of the International Forum on Aeroelasticity and Structural Dynamics – IFASD 2003, 2003

[23] Amprikidis, M., Cooper, J., "Adaptive internal structures for active aeroelastic control", Proceedings of the International Forum on Aeroelasticity and Structural Dynamics – IFASD 2003, 2003

[24] Rocha, J., Moniz, P., Costa, A., Suleman, A., "On Active Aeroelastic Control of na Adaptive Wing using Piezoelectric Actuators", Journal of Aircraft, Vol.41, N. 6, November-December, 2004

[25] Costa, A., "Novel Concepts for Piezoelectric Actuated Adaptive Aeroelastic Aircraft Structures", PhD Thesis, Instituto Superior Técnico, Portugal, 2002

[26] Rocha, J., Suleman, A., Costa, A., Moniz, P., Santos, D., "Research and Development of an Active Aeroelastic Adaptive Flight Demonstrator", CEAS/AIAA/ NVvL IFASD 2003, Netherlands, 2003

[27] Rocha, J., "An Experimental Study and Flight Testing of Active Aeroelastic Aircraft Wing Structures", MASc Thesis, University of Victoria, Canada, 2005

[28] Breitbach, E.J., "Research status on adaptive structures in Europe", 2nd Joint Japan-US Conference on Adaptive Structures, 1991

[29] Kauffman, G., Isaac, M., "Memory Metal", Chem Matters, 4-7, 1993.

[30] "Magnetostriction and Magnetostrictive Materials", (n.d.), Retrieved February 5, 2007, from http://aml.seas.ucla.edu/research/areas/magnetostrictive/mag-composites/Magnetostriction%20and%20Magnetostrictive%20Materials.htm

[31] "Piezoelectric Materials", (n.d.), Retrieved February 5, 2007, from http://www.piezomaterials.com

[32] "electrostriction." Encyclopædia Britannica. 2006. Encyclopædia Britannica Premium Service. 19 July 2006

[33] Stangroom, J.E.,"Electrorheological Fluids", Phys. Technol. 14: 290-296, 1983

[34] Jolly, M. R., Bender, J. W., Carlson. D. J., "Properties and Applications of Commercial Magnetorheological Fluids", SPIE 5th Annual Int Symposium on Smart Structures and Materials, 1998

[35] Ong, C, Tsai, S.W., "Design, Manufacture and Testing of a Bend-Twist D-Spar", Department of Aeronautics & Astronautics, Stanford University, SAND99-1324, 1999

[36] Cesnik, C.S, Shin, S., "On the twist performance of a multiple-cell active helicopter blade", Department of Aeronautics & Astronautics, MIT, 1999

[37] Garfinkle, M., Pastore, C., "Intrinsically-Smart Coupled Box Beams", Retrieved February 5, 2007, from http://www.pages.drexel.edu/~garfinkm/Spar.html

[38] M. Garfinkle - United States Patent 5,269,657 Aerodynamically Stable Airfoil Spar; Dec 1993 - All rights Reserved

[39] Atanasoff, H., Vizzini, A., "A Mfg. Process for Open-Mould Mechanically Coupled Composite Box Beams with Foam Tooling", AIAA/ASME/AHS/ASC, 28th Structures, Structural Dynamics & Materials Conf, 1989

[40] Corso, L., Popelka, D., Nixon, M., "Design, Analysis and Test of a Composite Tailored Tiltrotor Wing", Am. Helicopter Soc., 53rd Annual Forum, Virginia Beach, VA, 29th April, 1997

[41] Greenhalgh, E.S., Pastore, C., Garfinkle, M., "A Continuous-Fibre Composite Wing Box-Beam Exhibiting Twist-Beam Coupling", Composite Engineering 3(1993)691

[42] Shirk, M., Hertz, T., Weisshaar, T., "Aeroelastic Tailoring - Theory, Practice and Promise", J. Aircraft, 23(1984)6

[43] "Subproblem Approximation Method",. (n.d.), Release 10.0 Documentation for ANSYS.

[44] "D-Optimal Designs", (n.d.), Retrieved February 5, 2007, from http://www.itl.nist.gov/div898/handbook/pri/section5/pri521.htm

[45] "EN4-Dynamics and Vibrations", Division of Engineering, Brown University, Retrieved February 5, 2007, from http://www.engin.brown.edu/courses/en4/notes/Forcedvibes/Forcedvibes.html

Appendix A

EQUIPMENT

A.1. OROS

This equipment is used to perform impulsive response testing. It has several applications but just one is used, specifically, FFT analysis.

The accelerometers are placed on the wing/spar tip. A hit is given and the free frequency response can be analyzed by software.

The accelerometer output signal is connected to the spectrum analyzer via de connector panel. All frequency analysis is performed by the spectrum analyzer, and the resulting data are sent to the PC via the PCMCIA interface card. Finally, data is presented and post processed in the OR25 software. The process is done in almost real-time.

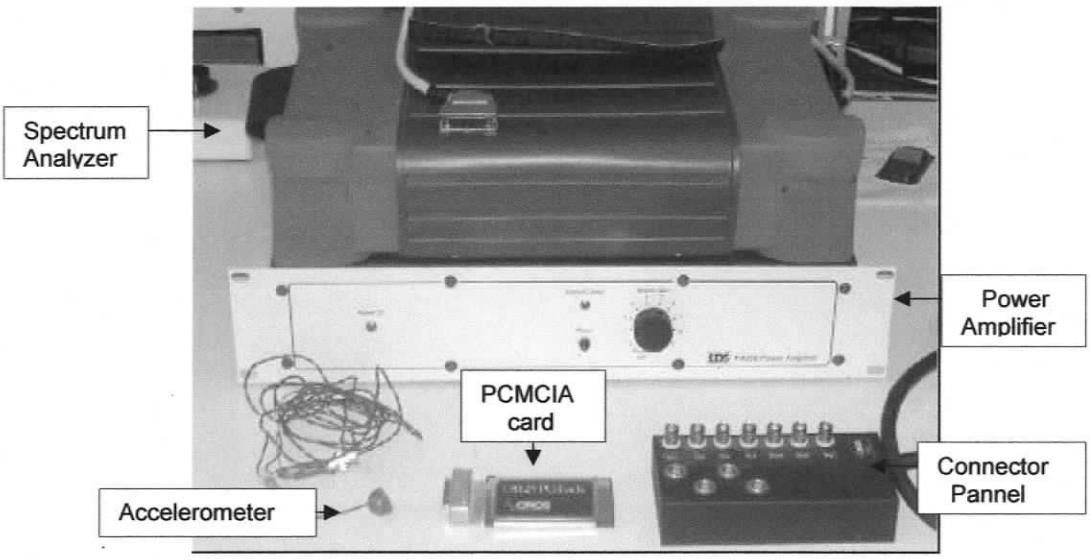

Figure A.1 OROS equipment

This system can be configured to find certain frequencies. This can be done by strategically placing the sensor. For example, if one aims to find vertical bending frequencies, the sensor should be placed on top of the structure.

A.2. Wind Tunnel

There is one wind tunnel installed at Portuguese Air Force Academy Aeronautical Laboratory. The wind tunnel is a closed circuit horizontal wind tunnel with a maximum operating velocity of 70m/s, with the air stream temperature control. The test section is 1.3m × 0.8m and 2m long, and can be used in an open or closed configuration. A uniform flow velocity with less than 0.8% in pressure variation can be obtained in a cubic zone 1.1m×0.6m×1.4m. The fan has 8 blades with 1.6m diameter. The shaft has a 0.63m diameter and rotates at maximum speed of 1600rpm, producing a maximum airflow of 72.8m3/s, with 88% efficiency.

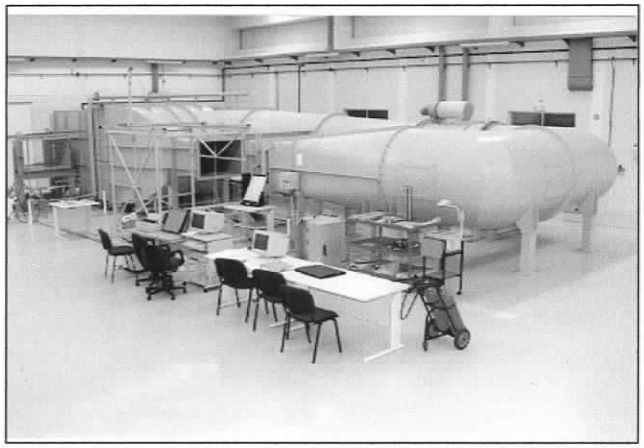

Figure A.2 Wind Tunnel Facilities

A model with a span of 1m can be used for wind tunnel tests with an open section configuration. The wing has to be clamped to a disk that allows rotation, which can simulate the variation of the RPV angle of attack.

A.3. Piezoelectric Actuators and Sensors

A.3.1. Sensor Characterization

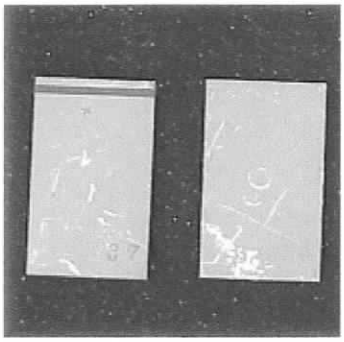

Figure A.3 BM500 PZT Sensors

The PZT sensors are 11×19 [mm] patches that become electrically charged when subjected to a mechanical strain, producing a variable ±2.5V AC electrical signal. Tables with characteristics are shown in the next figure.

		BM500	UNITS
Electrical[1]			
Relative Dielectric Constant	$K_{33}T$	1750	---
Dissipation Factor		1.6	%
Piezoelectric			
Coupling Factor	k_p	0.62	---
	k_{31}	0.37	---
	k_{33}	0.72	---
Charge Constant	d_{31}	-160	10^{-12}C/N
	d_{33}	365	10^{-12}C/N
Voltage Constant	g_{31}	-11.5	10^{-3}Vm/N
	g_{33}	25	10^{-3}Vm/N
Mechanical Quality Factor	Q_M	80	---
Frequency Constants[2]	N_p	2050	Hz.m
	N_1	1400	Hz.m
	N_3	1800	Hz.m
Elastic Modulus			
Compliance	S_{11}^E	15.5	$10^{-12}m^2/N$
	S_{33}^E	19.0	$10^{-12}m^2/N$
Density		7.65	g/cm^3
Curie Temperature	T_C	360	°C
Ageing Characteristics[3]			
Coupling Factor	k_p	-0.5	---
Dielectric Constant	K_{33T}	-1.0	---
Frequency Constant	N_p	0.5	Hz.m

Figure A.4 PZT Sensor Characteristics

Property	BM500
k15	0.680
d15	$575x10^{-12}$C/N
g15	$37.5x10^{-3}$ Vm/N
n15	1280 Hz.m

Figure A.5 Shear Mode Constants of PZT Ceramic

A.3.2. Actuator Characterization

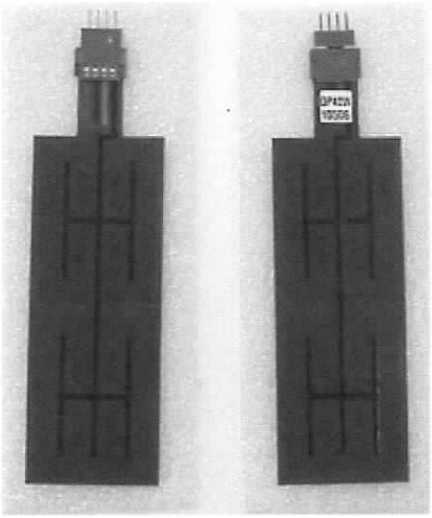

Figure A.6 ACX QP-40W PZT Actuators

The PZT actuators used were 2 pairs of ACX QP-40W actuators, each pair bonded on upper and lower spar surfaces.

The ACX QuickPack 40W actuator used is built through a proprietary manufacturing process that shields the PZT material in a protective polyamide coating with pre-attached electrical leads and quick connectors, improving electrical isolation and adding protection against breakage during assembly and resistance to micro cracks during operation. This process also allows that 4 PZT patches to be packed, in order to be used in serial, to increase actuation mechanical energy.

ACX guarantees a proper frequency response of the actuator for input signals with frequencies between $1Hz$ and $20kHz$.

The QP-40W electromechanical characteristics are given on the following figure:

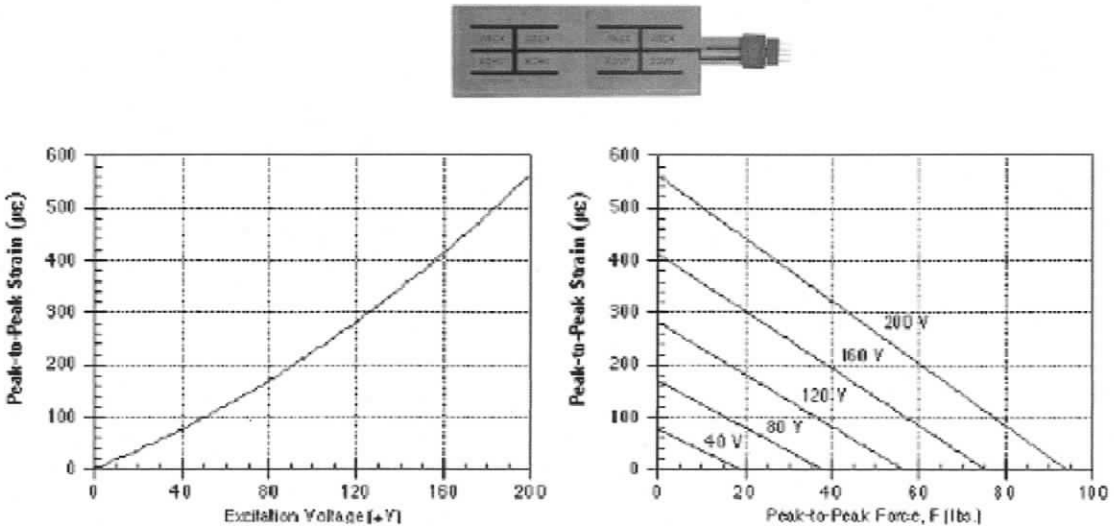

Figure A.7 ACX QP-40W Actuators Electromechanical Characteristics

A.4. Electronic Gear

A digital control module is required to fulfill the desired purposes and it has different roles depending on the application. For vibration reduction, a control law can be uploaded and the output for the actuators is a function of the sensors input. For frequency based health monitoring, it must read the sensors input and compare them with undamaged structural response, previously stored. For wave propagation methods, it must control the actuators pulses (type, frequency and amplitude) and read the sensors responses, also comparing them with undamaged structural response, previously stored. On both methods, after the comparison, algorithms will be implemented to access the location and type of damage. On all cases, the electronics to be applied will be the same. This will be an advantage since only one electronic apparatus will be used to apply the three control methods.

The entire hardware system to be used for experimental ground tests (spar and wing), wind tunnel and flight testing is shown below:

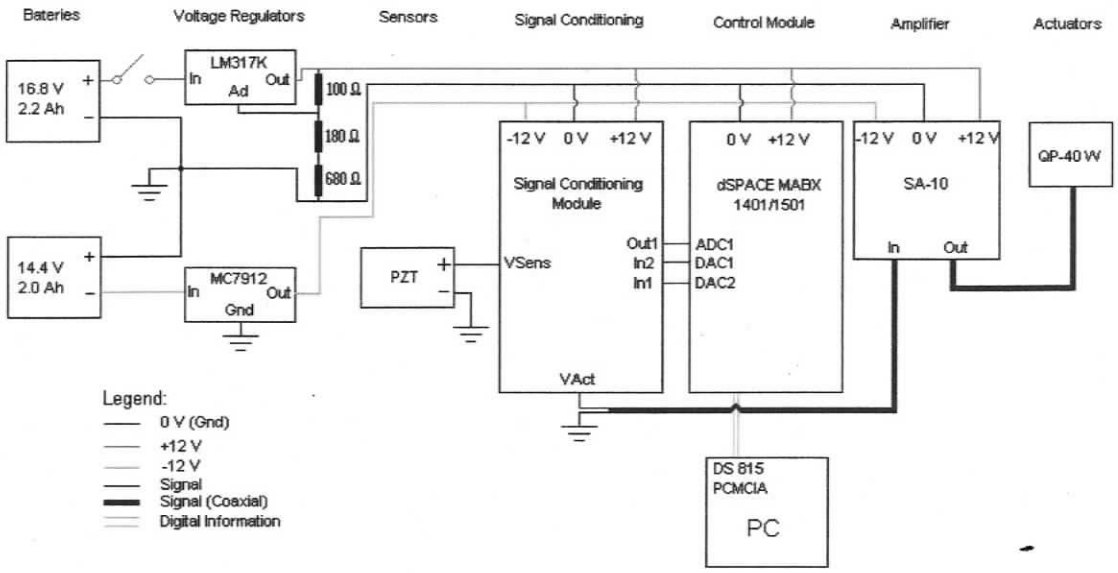

Figure A.8 Hardware Blocks and Connections

The figure highlights the connections between all hardware blocks, which were developed and assembled in a modular way. These connections are detailed in the figure's legend and include power, signal and digital information flux. All blocks were disposed by functional levels (batteries, voltage regulators, sensors, signal conditioning, control, amplifier and actuators), and will be exposed next with more detail.

A.4.1. The Amplifiers

The external amplifier is a "ACX 1224/5 QuickPack", specially designed to be used with the QuickPack actuators applied. It accepts an input signal and amplifies it to provide an output of up to ±200V, peak. It features adjustable inverted gain from 1x to 20x continuous, selectable voltage ±100V or ±200V and output current limit 50mA or 200mA. It's powered by 220V AC.

Figure A.9 ACX 1224/5 Amplifier

The internal amplifier is a modified "Sensor Technology SA-10 High-Voltage Power Amplifier" that can be used as two individual ground-referenced amplifiers each one with a 15 times gain. The total input voltage is limited to approximately ±9V, setting the output to a maximum voltage swing of ±140V (RL = 100k). The maximum output current (per channel) is internally limited to 50mA. The amplifier Slew Rate is 3.8V/µs (RL = 3k). One of the foremost advantages of the modified amplifier is it's weight of only 100g and the small dimensions of 1" x 3" x 5".

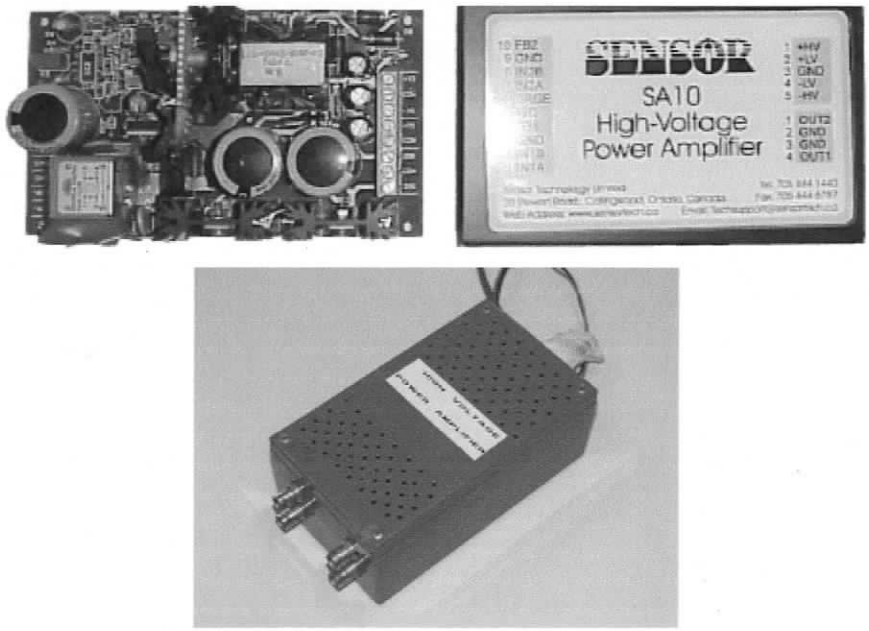

Figure A.10 SA-10 Amplifier Components and Flight Test Container

A.4.2. Control Module

The digital control module used for now is the DSPACE MicroAutoBox 1401/1501. It is the most important equipment in the experimental setup, and it weighs 1022 g. The DS 1401 Base Board is based on the PowerPC 603e processor (PPC) that forms the main processing unit of the MicroAutoBox.

The DS1401/1501 boards were packed in a metallic case with cooling vanes, and the case is too wide to fit the RPV. The case was removed, and the PPC was tested in order to see if the working temperature didn't overcome the maximum temperature (85°C). It was decided to install one heat exchanger over the processor, and the temperature read, with the entire system working, never exceeded 50°C. So, the board behaviour was never affected by the accumulated heat.

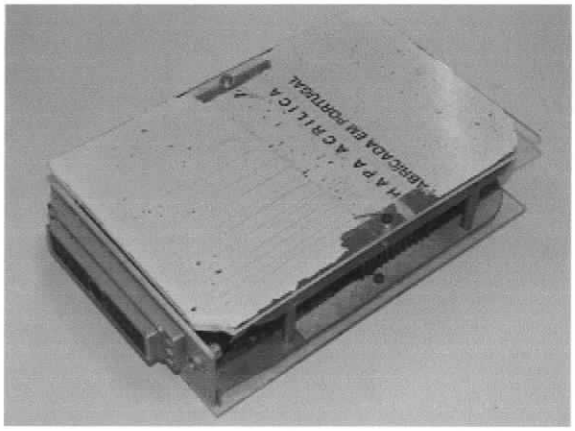

Figure A.11 DSPACE Module Without Casing for Flight Testing

A.4.3. Signal Conditioning

The need for signal conditioning arises from the fact that the output voltage signals from the sensors (-2.5/+2.5V) are incompatible with the input voltage signals from the DS1501 (0/+5V), and also the voltage signals from DS1501 (0/+4.5V) need to be modified to fit SA-10 amplifier voltage input signals (±9V), in order to achieve the amplifier's

maximum output voltage to feed the actuators. On the other hand the signal before the SA-10 amplifier must have the DC component removed. The option of trying to use the maximum output voltage of the actuators is justified to achieve the maximum output energy with the minimum controller gain, in order to achieve high strain rate control at higher frequency demands.

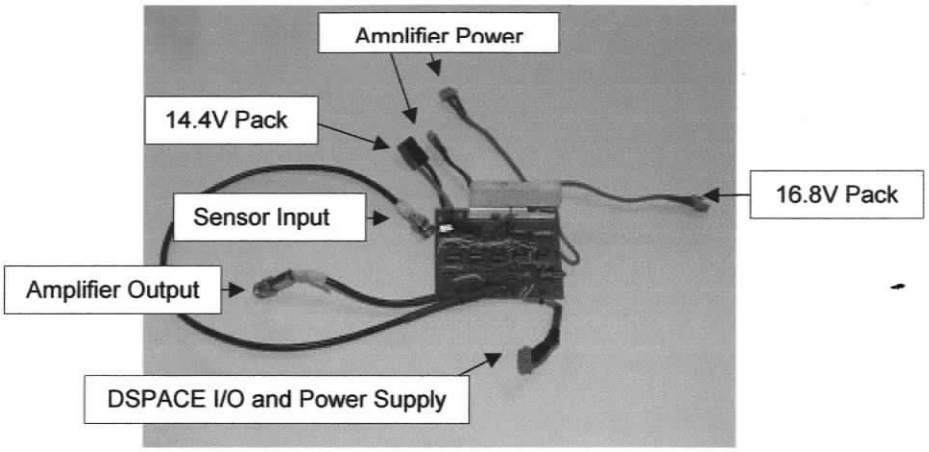

Figure A.12 Signal Conditioning Module and Connectors

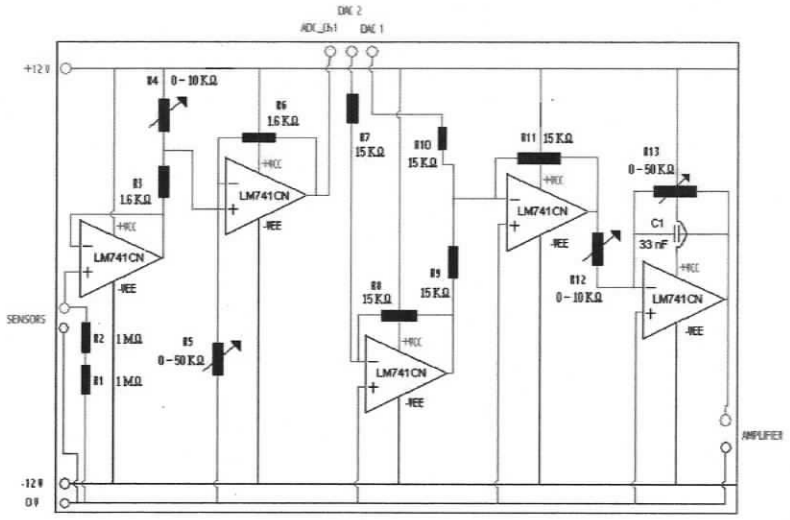

Figure A.13 Signal Conditioning Schematics

As it was decided to limit to the minimum the operations performed by hardware components, although they are faster and more efficient, because of volume/weight

restrictions of the RPV, the main responsibility of performing filtering and control operations was left to software modules running on the PPC. This option has to be accessed to check for high frequency response and delays introduced by the system in the loop. Therefore, the circuit between DS1501 and SA-10 was modified in order to avoid using too many OpAmp's (with stability and quality problems), and to add flexibility to the control law implementation. The controller output signal was separated into positive and negative part, and two DAC channels were used (with limited output between 0/+4.5V). This option has an overall output voltage range of -4.5/4.5V and doesn't need a large pre-amplification value prior the SA-10 power amplifier. The main piece in the circuit is the 741 Operational Amplifier. It needs two power signals (+VCC and –VEE). Normally +VCC = VEE and lies between 5 and 15V. The value of +VCC = VEE =12V was chosen for this work, to be compatible with DSPACE and SA-10 power supply inputs. This component doesn't have a GND terminal, and sometimes a ground adjustment may be needed.

A.4.4. Functions Description

The first operational amplifier is a circuit referred to as a voltage follower, being in the ideal case V0 = Vi; Rin = 1 and Rout = 0. This montage is needed to function as a buffer between the high impedance source (PZT sensors) and the low-impedance load (current thought R1 and R2). The second operational amplifier is the superposition of a noninverting configuration with a weighted summer, and is intended to add a 2.5V DC offset to the sensor signal.

As the controller command signal is separated in positive and negative parts, the positive part is driven through the DAC channel 1, and the negative component is inverted and driven to DAC channel 2. This way the 3rd amplifier is the channel 2 inverter, the 4th OpAmp is the weighted summer of channel 1 and 2 (with unity weights) and the last one works as result inverter, pre-amplifier (by a factor slightly superior than -4).

A.4.5. Power Supply

Although a lot of testing in the wind tunnel is to be conducted with the energy supply provided by a TTi power supply, the final wind tunnel tests should be performed with two batteries in serial connection. The positive terminal of the first battery and the negative terminal of the second battery provide the reference signal for all equipments (GND).

The first one is a PowerfLlite14.4V, 2000 mAh lithium-ion pack. It is used to provide voltage and current to the -12V voltage regulator, in order to feed de -12V amplifier and signal conditioning circuit inputs. As it is feeding the negative part of the circuits, it needs to provide low output current values (0.1 A), making the endurance to rise to over 2h30m in continuous working mode. This pack weighs 205 g.

To feed the +12 V input of the amplifier, signal conditioning circuit and DS1401 (the most demanding component in terms of current), a 16.8 V NEXcell, 2.2 mAh and 428 g pack is used, connected to a voltage regulator.

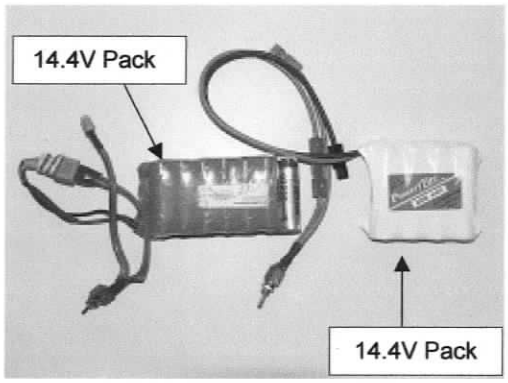

Figure A.14 Battery Packs

To feed these components, this battery has to continuously provide 1.2A, and more than 2.05A peak, due to the transient input peak due to dS1401 start-up. Therefore, it is the critical electrical component in terms of endurance. As this was the only way to turn the DS1401 ON and OFF, one interrupter was installed. A fuse was also installed to protect the circuits from over current.

A.4.6. Voltage Regulators

A stable voltage power supply is a fundamental requirement of all components (the 741 OpAmp and SA-10 work with -12 and +12V, and DS1402 works with +12V), it was decided to include voltage regulators in the hardware components, between the two batteries and the signal conditioning circuit. The selected components were MC7912 e LM317K:

- MC7912 - This component provides, on its output gate, a stable voltage of -12V. It allows current loads 1A. It is manufactured by Samsung GmbH;
- LM317K - On the other hand, this one provides, on its output gate, a stable voltage of +12V. It works with current loads up to 3A. It is manufactured by Thomson GmbH. As this component deals with relatively high values of power, it was necessary to adapt one heat exchanger, as shown in figure A.12 The auxiliary resistor values were found in the component datasheet.

A.4.7. Software

In order to use the DSPACE control module, MATLAB and DSPACE Control Desktop are required. The last one allows for controlling the DSPACE in every aspect. MATLAB is vital because any program designed to be uploaded to the DSPACE must be firstly implemented through SIMULINK then compiled and lastly uploaded to the module. After this procedure, DSPACE Control Desktop can be used to change any inputs and monitor the output of the program.

The DSPACE has to be connected to Personal Computer (PC) in order to be configured. It can be used as a stand-alone unit as long as a program is uploaded into it. In this case, whenever it's turned on it will execute that program and will save any data related to it for future download, if desired.

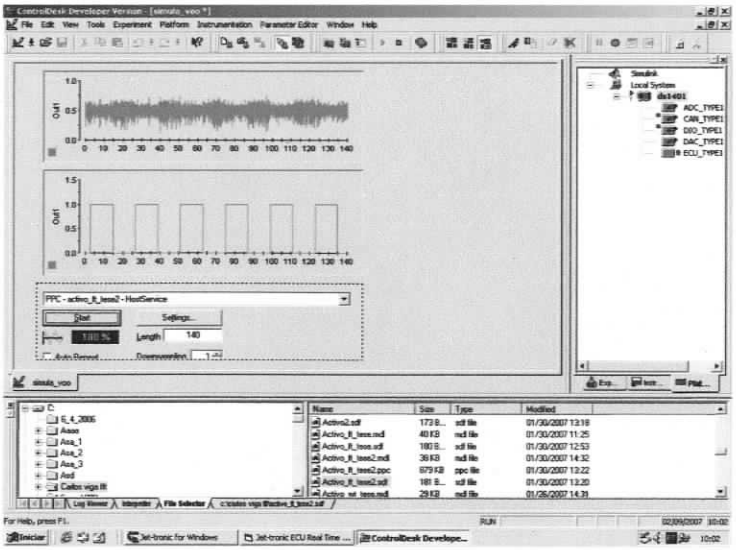

Figure A.15 DSPACE Control Desktop Layout Window

A.5. Flight test equipment

A.5.1. RPV

This platform is ideal to test the technology developed. It was designed in such way that allows installation of different wings, with the only restriction of having a compatible wing-fuselage fitting. Its Maximum Take-Off Weight (MTOW) and fuselage available volume are suitable for the required gear necessary to perform the flight tests. Another important aspect is the flight envelope. The speeds selected to do the flight testing are between the minimum speed (Stall speed) and the maximum one, below to the predicted flutter speed. The RPV possesses telemetry equipment that is capable of tracking the Indicated Air Speed (IAS).

To better elucidate the RPV characteristics the following pictures and data tables are presented.

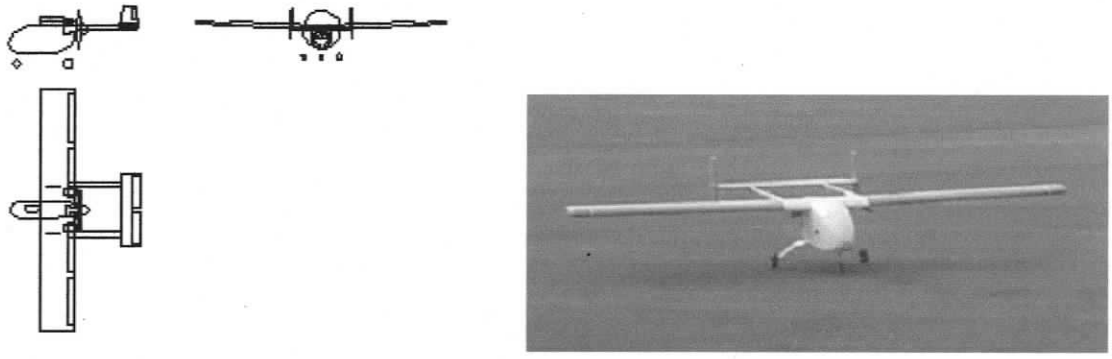

Figure A.16 RPV Sketch Views and Photograph

Table A.1 RPV Geometric Characteristics

Parameter	SI Units
Main Wing Span	2.4 m
Main Wing Chord (Root)	0.33 m
Main Wing Chord (Tip)	0.33 m
Main Wing Aspect Ratio	7.273
Horizontal Stabilizer Span	0.72 m
Horizontal Stabilizer Chord (Root)	0.18 m
Horizontal Stabilizer Chord (Tip)	0.18 m
Horizontal Stabilizer Aspect Ratio	4
Vertical Stabilizer Span	0.2 m
Vertical Stabilizer Chord (Root)	0.184 m
Vertical Stabilizer Chord (Tip)	0.138 m
Vertical Stabilizer Aspect Ratio	1.242
Wheel Track	0.3713 m
Wheel Base	0.5048 m
Propeller Diameter	0.38 m

Table A.2 RPV Areas

Parameter	SI Units (m^2)
Main Wing Area. Gross	0.792
Flaps Area	0.06336
Ailerons Area	0.06336
Horizontal Stabilizer Area. Gross	0.1296
Elevator Area	0.03786
Vertical Stabilizer Area. Gross	0.0644
Rudder Area	0.007491

Table A.3 RPV Wing Loading and Power Characteristics

Parameter	**SI Units**
Max Wing Loading	12.63 Kg/m^2
Max Power Loading	0.00537 Kg/Watts

Table A.4 RPV Performance Characteristics

Parameter	**SI Units (m/s)**
Max Level Speed (SL)	42.02
Cruise Speed (SL. 75% Power)	38.6
Stall Speed Clean (Power On)	15.81
Stall Speed 45. deg Flaps (Power On)	12.39
Max Rate of Climb	8.44

A.5.2. Airborne equipment

All the equipment used in the Wind Tunnel tests has to be on board. The DSPACE is responsible for carrying out the active system control and data storage. The signal conditioning module and amplifier are also required. On top of this, a set of batteries has to be carried to provide power to the remote control unit, active control and storage system and finally to the telemetry system.

On the ground, a laptop is required to gather the information transmitted by the telemetry system and a remote control unit to guide the RPV.

All the above gear is explained in more detail on the following sections.

Telemetry Subsystem

During flight tests, it is mandatory to have information about the RPV airspeed. A telemetry system with bidirectional datalink is installed in the RPV. The speed readings have to be previously calibrated in the wind tunnel, comparing with the tunnel speed

measurement. The available system was originally designed to be a model aircraft turbine ECU (Engine Control Unit), and the only used function is the speed information. The components of this subsystem are:

- JetCat Jet-tronic II P-80 ECU microcomputer –performs the signal conditioning, and RF (Radio Frequency) modulation operations; it is connected to the battery back, pitot's transducer, air station transceiver and onboard radio control receiver;
- JetCat 7.2 V, 1250 mAh, 6 cell Ni-Cd battery pack, that supplies power to the airborne station via ECU;
- Pitot-static (total pressure and static pressure inputs) sensor, with transducer to convert pressure in electronic signal, and PPM (Pulse Position Modulation) modulator;
- ECU transceiver with antenna – sends radio signal to the ground station;
- Mini Ds-IPD radio-control receiver – this 9 channel, FM-IPD-PPM narrowband receiver (with 10 kHz channel spacing) works with the flight control surfaces, and it is used connected to the ECU by the auxiliary and throttle channels, being fundamental for the proper functioning of the ECU; it has independent battery pack.

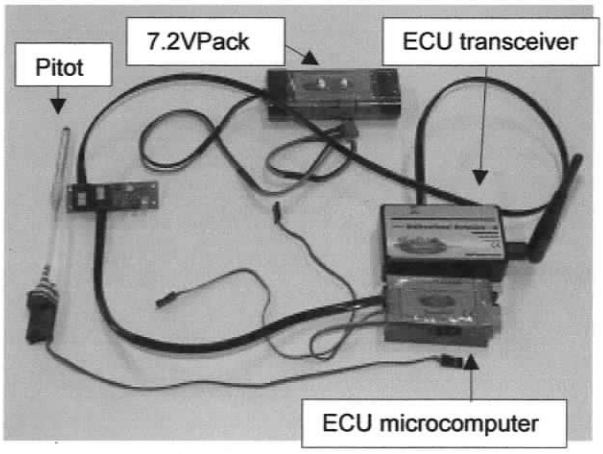

Figure A.17JetCat Flight Test Components

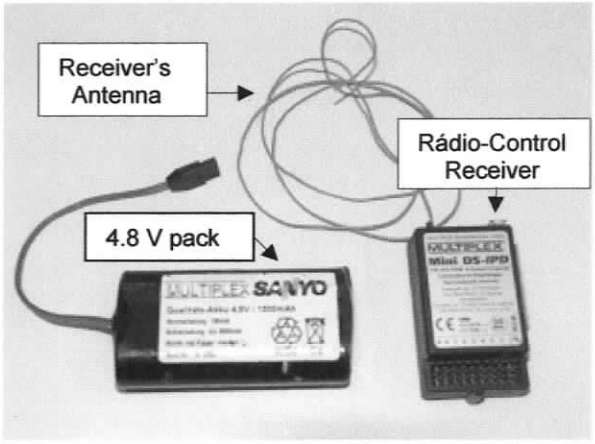

Figure A.18 Receiver and Battery Pack for Flight Testing

A.5.3. Ground equipment

The ground station components are:

- Ground station transceiver – receives the radio signals from the aircraft; it is connected to the PC by the USB slot (power) and RS232 serial adapter (Data);
- Profi mc 4000, 16 bit FM-PPM/PCM radio-control unit – the telemetry system doesn't work unless the radio-control unit is turned on, other wise the radio control receiver may become damaged.

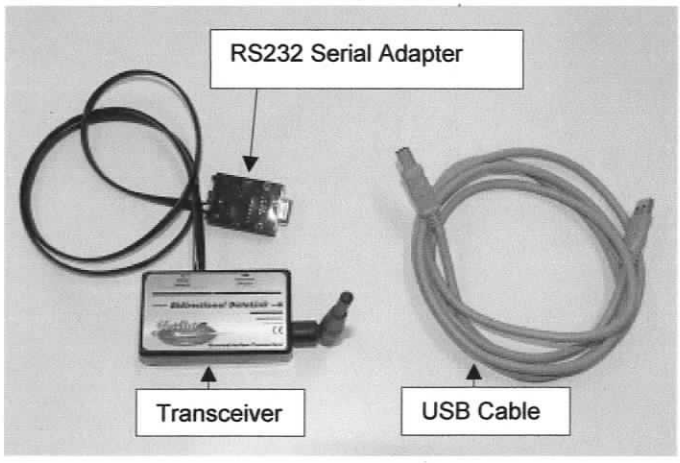

Figure A.19 JetCat Ground Components

Figure A.20 Radio Control Unit

A.5.4. Software

The software used to monitor the airspeed of the RPV is the Jet-tronic II. This program has a data display windows that allows monitoring the IAS, between other options.

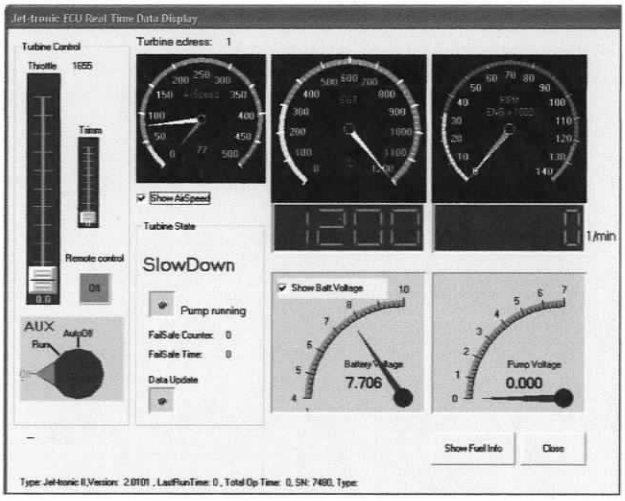

Figure A.21 Jet-Tronic ECU Real Tome Data Display Window

The previous figure illustrates the Data Display window. It shows throttle and trim controls position, fuel pump voltage, engine RPM and EGT (Exhaust Gas Temperature), and airspeed and battery voltage. The last two functions were the only ones used.